Revista
GEOCIÊNCIAS

unesp

ISSN: 1980-900X (online)

STRUCTURAL TRAPPING AND INTERNAL GEOMETRY OF FRACTURED CARBONATE RESERVOIRS: A CASE STUDY IN THE IRATI FORMATION, SALTINHO (SP), BRAZIL

TRAPEAMENTO ESTRUTURAL E GEOMETRIA INTERNA DE RESERVATÓRIOS CARBONÁTICOS FRATURADOS: UM ESTUDO DE CASO NA FORMAÇÃO IRATI, SALTINHO (SP), BRASIL

Saul Hartmann RIFFEL[1], Viviane Barbosa GIMENEZ[2], Norberto MORALES[1], Iata Anderson de SOUZA[1], Leonardo Fadel CURY[3], George Luiz LUVIZOTTO[1]

[1]São Paulo State University (UNESP), Institute of Geosciences and Exact Sciences, Rio Claro. E-mails: saulriffel@gmail.com; n.morales@unesp.br; iata.anderson@gmail.com; george.luvizotto@unesp.br

[2]Centro de Estudos de Petróleo (CEPETRO), Universidade Estadual de Campinas (UNICAMP), Campinas, SP, Brasil. E-mail: vivianebgimenez@yahoo.com.br

[3]Department of Geology, Institute of Mineral and Rock Analysis Laboratory, Federal University of Paraná, Centro Politécnico, Curitiba, PR, 81531-980, Brazil. E-mail: cury@ufpr.br

ABSTRACT - The evolution of structural traps in fractured carbonate reservoirs is governed by fault-zone architecture, which controls permeability, fluid pathways, and trap preservation through time. In the Irati Formation, on the eastern margin of the Paraná Sedimentary Basin (Brazil), normal faults compartmentalize a dolomitic succession that hosts outcrop-scale hydrocarbon accumulations. Irati dolomites represent an unconventional fractured reservoir in which hydrocarbon generation, storage, and trapping occur within the same stratigraphic interval, controlled by secondary porosity and multi-nucleated fault zones. This study examines how such reservoir behaviour is linked to the evolution of fault-zone architecture by integrating structural characterization, paleostress analysis, and U–Pb dating of syntectonic calcite to constrain the timing and conditions of brittle deformation and fluid circulation. Our results show that an early extensional phase (~74 Ma) produced a fracture network in a laterally connected damage-zone, establishing conduit-dominated flow along the dolomitic layer. Subsequent Cretaceous post-rift reactivation promoted fault-core sealing through brecciation, clay smearing, and calcite precipitation, sharply reducing cross-fault permeability and consolidating a structural trap during the Late Cretaceous (~75 Ma). A younger Paleogene event (~35 Ma) generated minor reactivation but did not breach the sealed core, demonstrating that reactivation alone does not necessarily compromise traps in mechanically layered systems. We propose a three-stage evolutionary model linking conduit formation, fault-core sealing, and trap preservation. These findings emphasize that the long-term hydrocarbon retention in the Irati system is primarily an architectural outcome, and highlight the value of integrating U–Pb carbonate geochronology with structural analysis to refine trapping models in fractured carbonate reservoirs in similar settings worldwide.
Keywords: Fractured carbonate reservoirs. Fault-zone architecture. Structural trap. U–Pb carbonate geochronology. Mechanical stratigraphy. Paraná Sedimentary Basin.

RESUMO - A evolução de trapas estruturais em reservatórios carbonáticos fraturados é definida pela arquitetura das zonas de falha, que controla a permeabilidade, o fluxo de fluidos e a preservação das trapas ao longo do tempo. Na Formação Irati (Permiano), margem leste da Bacia Sedimentar do Paraná (Brasil), falhas normais compartimentalizam uma sucessão dolomítica que preserva impregnações de hidrocarbonetos em escala de afloramento. Os dolomitos da Formação Irati representam um reservatório não-convencional fraturado, no qual geração, armazenamento e aprisionamento ocorrem dentro do mesmo intervalo estratigráfico, controlados pela porosidade secundária e por zonas de falha multinucleadas. Este estudo investiga como esse comportamento de reservatório está relacionado à evolução da arquitetura das zonas de falha, integrando caracterização estrutural, análise de paleoesforços e datações U–Pb LA-ICP-MS em calcita sintectônica para reconstruir o contexto temporal e a influência da deformação rúptil na circulação de fluidos. Os resultados indicam que uma fase distensiva inicial produziu uma rede lateralmente conectada de fraturas na zona de dano, estabelecendo caminhos preferenciais de fluxo na camada dolomítica. Reativações pós-rifte subsequentes durante o Cretáceo e Cenozoico promoveram o selamento do núcleo da falha por brechamento, folhelho cominuído e precipitação de calcita, reduzindo drasticamente a permeabilidade lateral e consolidando uma trapa estrutural no Cretáceo Superior (~75 Ma). Um evento rúptil mais jovem, no Paleógeno (~35 Ma), gerou reativações discretas sem rompimento do núcleo selado, demonstrando que reativações posteriores não necessariamente implicam comprometimento de trapas em sistemas mecanicamente anisotrópicos. O modelo evolutivo proposto evidencia que a retenção de hidrocarbonetos no sistema Irati é, sobretudo, um resultado arquitetural, e ressalta a importância de integrar geocronologia U–Pb em carbonatos e análise estrutural para aprimorar modelos de trapa em reservatórios carbonáticos fraturados em contextos análogos.
Palavras-chave: Reservatórios carbonáticos fraturados. Zonas de falha. Trapas estruturais. Geocronologia U–Pb em carbonatos. Estratigrafia mecânica. Bacia Sedimentar do Paraná.

INTRODUCTION

In unconventional petroleum systems, hydrocarbon retention and deliverability are governed less by classic buoyancy-driven migration and more by the configuration of low-permeability layers, capillary thresholds, and mechanically guided flow paths (Zou et al., 2013). Fault systems exert a primary control on fluid migration and trapping in fractured carbonate reservoirs, where permeability is strongly heterogeneous and largely dictated by structural elements at multiple scales (Sibson, 1990; Caine et al., 1996).

Depending on their internal architecture, fault zones may alternate between high-permeability conduits and low-permeability barriers, thus governing whether fluids are able to escape, accumulate, or become permanently sealed within specific stratigraphic levels (Evans, 1990; Antonellini & Aydin, 1994). Despite major advances in structural diagenesis and fracture-controlled flow, a fundamental question remains insufficiently resolved: how does permeability evolve through successive brittle reactivation events, and at what stage does a structural trap become fully effective?

Carbonate reservoirs are particularly sensitive to this question because they tend to develop complex fracture networks, dissolution surfaces, stylolites, cementation phases and veining that can either enhance or reduce permeability over geological timescales (Laubach et al., 2019). In many case studies, however, the chronology of fracture activity and fault sealing remains inferred rather than demonstrated, due to the scarcity of absolute age constraints on brittle deformation and fluid circulation (Sibson, 1994; 1996; Jourde et al., 2002). As a result, structural traps in carbonates are frequently interpreted based on geometry alone, leaving a significant temporal gap: we often know *how* faults trapped fluids, but not *when* the trapping architecture became effective or how long it remained hydraulically intact.

The Irati Formation in southeastern Brazil, on the eastern margin of the Paraná Basin, offers a unique natural laboratory to address this issue. Organic-rich shales and dolomitic carbonate beds host hydrocarbon accumulations in outcrop, spatially confined within a fractured dolomitic horizon bounded and crosscut by normal faults.

This scenario provides an exceptionally rare opportunity to investigate the interplay between fault architecture, fracture connectivity and fluid trapping at outcrop scale, rather than in subsurface datasets where geometries and internal fabrics are inferred indirectly (Araújo et al., 2000; Milani, 2007).

In the Saltinho area, these faults deforming the Permian Irati Formation formed initially during the Early Cretaceous regional extension associated with the rift event that caused the breakup of the Gondwana Supercontinent, and were later affected by post-rift intraplate reactivation, producing multiple deformation episodes that directly influenced reservoir permeability over time (Riccomini, 1995; Zalán & Oliveira, 2005).

Although previous structural studies in the region have documented normal faults striking predominantly NW–SE and consistent extensional stress fields, no temporal model has yet constrained the evolution of structural trapping in the Irati carbonates. The outcrop clearly preserves damage-zone fracture networks, sealing fault cores, hydrocarbon confinement, multiphase mineralization, and reactivation features — but the timing of these events has remained speculative.

Recent advances in U–Pb geochronology of syntectonic calcite now allow direct dating of brittle deformation and fluid circulation (Roberts et al., 2020; Nuriel et al., 2017), providing a powerful tool to resolve this missing temporal dimension. By integrating structural observations with absolute age constraints, it becomes possible to reconstruct when fractures were open and conductive, when fault cores became sealing, and whether later reactivation breached or instead reinforced structural traps.

Here we integrate structural analysis, paleostress inversion, and U–Pb dating of syntectonic calcite to unravel how brittle fault reactivation governed fluid pathways and ultimately consolidated a post-rift structural trap in the Irati carbonates near the Saltinho municipality (São Paulo). This approach establishes a process-based evolutionary model in which permeability, hydrocarbon migration, sealing, and long-term trap preservation are intrinsically related with the tectonic history of the fault system.

GEOLOGICAL AND TECTONIC SETTING

The Paraná Basin is one of the largest Paleozoic–Mesozoic sedimentary basins in southwestern Gondwana, recording multiple supersequences associated with recurrent phases of subsidence, magmatism, and tectonic reactivation (Milani et al., 1994, 1997, 2007). During the Early Cretaceous, the evolution of the South Atlantic rift system imposed significant extensional deformation on the eastern margin of the basin (Zalán et al., 1990; Zalán & Oliveira, 2005). The breakup of Gondwana generated a NE–SW to ENE–WSW extensional stress field that promoted normal faulting and reactivation of preexisting anisotropies within the Paraná Basin sedimentary filling, particularly along NW–SE structural trends. In the studied region, these structures accommodated syn-rift normal faulting, fragmenting the Irati Formation layers and establishing the first generation of fracture networks that would later influence fluid migration and compartmentalization.

Following continental breakup, the region evolved into an intraplate continental margin subjected to successive deformation episodes. Far-field stresses associated with Andean orogenesis, changes in plate boundary forces, and ridge-push effects led to repeated reactivation of Brazilian Precambrian basement fabrics and Cretaceous rift-related faults (Riccomini, 1995; Hackspacher et al., 2004). These post-rift episodes generated multiphase brittle reactivation expressed as renewed normal faulting, oblique-slip kinematics, and reorganization of fracture networks across southeastern Brazil, including the eastern Paraná Basin. Importantly, such reactivations occurred under episodic stress fields during the Late Cretaceous and Paleogene (Gimenez et al., 2022; Salamuni et al., 2021; Santos et al., 2023), providing multiple windows for fluid circulation, sealing or breaching of traps, and hydrocarbon redistribution through time.

Our target region is located in a structural domain marked by a series of basement-controlled structures, including the Pitanga, Pau d'Alho, Artemis and Jibóia structures (Soares, 1974), the latter encompassing the area investigated in this work (Figure 1). These structural blocks trend predominantly NW–SE, reflecting the influence of the Tietê Lineament, whose expression can be traced from faults and deformation zones in the crystalline basement near Itu into the overlying sedimentary succession. This tectonic inheritance compartmentalizes the basin and exerts first-order control on stratigraphic distribution, fluid pathways and structural trapping.

Stratigraphically, the studied successions lie within the Passa Dois Group, whose infill comprises mainly marine to continental deposits, with the Permian section marking the transition from glaciogenic environments to restricted marine conditions. Within this framework, the Irati Formation represents a major anoxic episode characterized by organic-rich shales and dolomitic carbonate layers deposited in a stratified, restricted marine basin with limited circulation – the Irati-Whitehill sea (Bastos et al., 2021; Soares, 1988; Araújo et al., 2000). The Irati Formation is subdivided into the Taquaral (base) and Assistência (top) members (Barbosa & Almeida, 1949), the Taquaral Member consisting of grey siltstones and dark grey to greenish shales (3–15 m thick), while the Assistência Member contains dolomitic limestones and subordinate pelites interbedded with bituminous shales, frequently bearing silica nodules and stromatolites. The thick dolomitic beds at the base of the Assistência Member host several quarrying operations in the studied region (e.g. Amaral Machado quarry). With an estimated average thickness of ~40 m, the Irati Formation sequences formed under low-energy conditions in a shallow marine to restricted lagoonal paleoenvironment (Schneider et al., 1974; Perinotto & Zaine, 2008). Palynological data indicate a Late Permian (Kazanian) age (Daemon & Quadros, 196), whereas zircon geochronology suggests an early Permian (Artinskian) age from dating of volcanic ash layers (Santos et al., 2006). Moreover, a zircon U–Pb TIMS age of 277.26 ± 0.62 Ma was attributed to the final evolutionary stages of the Irati–Whitehill water body, capturing the transition toward a progressively restricted depositional system in the Paraná Basin (Bastos et al., 2021).

Being a key stratigraphic marker in the Paraná Basin due to its fossil assemblages (e.g., Mesosaurus, Stereosternum, crustaceans and palynomorphs) and its tectonic stability during deposition (Simões & Fittipaldi, 1992), the Irati Formation also represents one of the most organic-rich units in the basin, with total organic carbon contents reaching up to 23% (Milani, 2007), being widely recognized as a major hydrocarbon source rock (Moraes Rego, 1930; Araújo et al., 2000; Lisboa, 2006; Cerri et al., 2020).

Hydrocarbon generation is closely linked to thermal input from Early Cretaceous intrusions of the Serra Geral magmatism (Thomaz Filho et al., 2008), and migration commonly reaches the Pirambóia Formation and, locally, units immediately above or below Irati, especially near fault

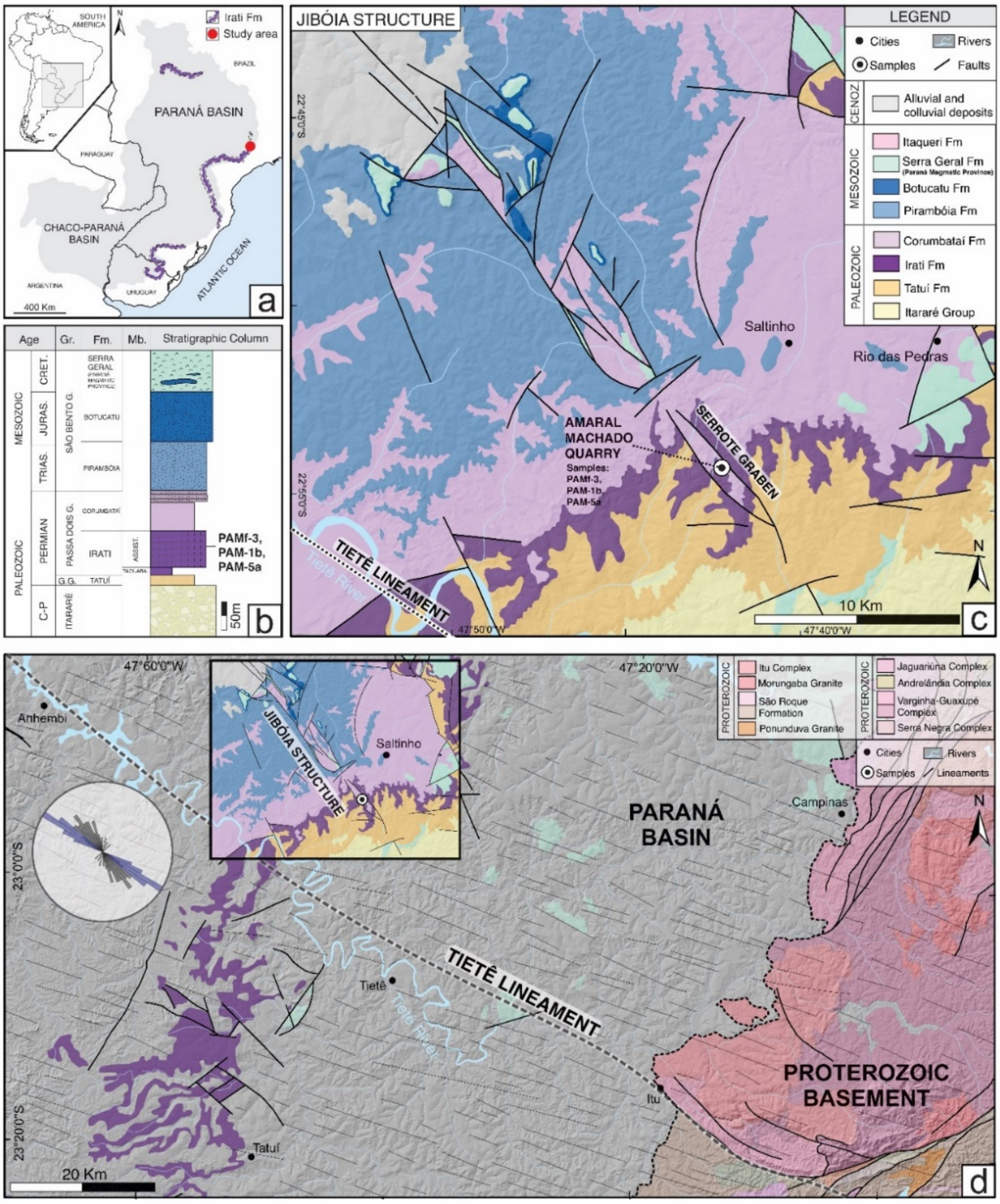

Figure 1 - Location and geological framework of the study area in the northeastern Paraná Basin. *(a)* Regional setting showing the distribution of the Irati Formation within the basin. The red dot indicates the approximate location of the studied area *(b)* Simplified stratigraphic column highlighting the dolomitic interval of the Irati Formation and sampled horizons. *(c)* Geological map of the Saltinho region,highligthing the Jiboia and Serrote structures, and Amaral Machado Quarry, showing major faults associated with the Tietê Lineament (modified from CPRM, 2019). *(d)* Regional structural context illustrating the relationship between the Jibóia structure and the Tietê Lineament, which follow the homonymous river crossing the SW border of the study area towards the Proterozoic crystalline basement near the municipality of Itu. NW-SE-trending lineaments are pervasive across the region, as shown in the rose diagram of main identified faults.

zones (Aquaroli, 2013; Mateus et al., 2014). In the Rio Claro-Piracicaba region, the interplay between organic-rich shales, dolomitic horizons and major structures (e.g. Serrote Graben, Jibóia Structure) favoured the development of unconventional fractured reservoirs and structural traps.

Within this tectonic context, the Irati Formation behaved as a mechanically layered reservoir analogue (Cerri et al., 2020), where contrasting rheologies between dolomitic beds and organic-rich shales favored the development of fault cores, relay structures, and asymmetric damage zones. The dolomitic layers, more competent and brittle, tended to fracture and host numerous vein systems, whereas the interbedded shales localized shear and contributed to low-permeability fault-core material.

These heterogeneities related to the mechanical stratigraphy exerted direct control on the mobilization of fluids during both syn-rift deformation and later post-rift reactivation events, a relationship that is clearly observable at outcrop scale in the Amaral Machado quarry (Figure 2).

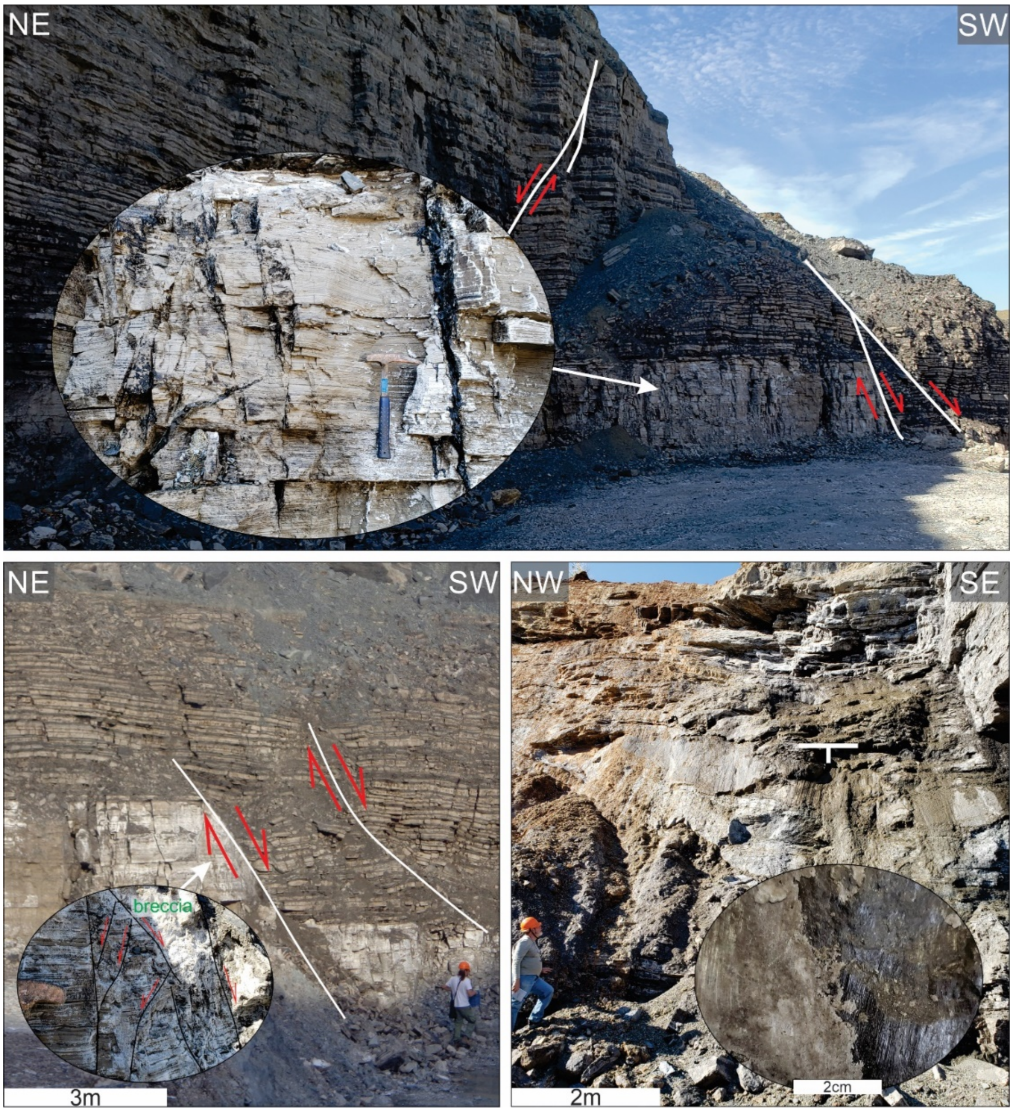

Figure 2 - Outcrop view of the fault zone in the dolomitic layers of the Irati Formation at the Amaral Machado Quarry (Saltinho - SP); *(a)* Overview of the main dolomitic layer showing fracture concentration with hydrocarbon; *(b)* One major fault within the zone with its breccia fault core; *(c)* Fault surface of shale smear with slickensides; *(d)* Detail of shale smear fault core with secondary calcite film.

Overall, the geological evolution of the region establishes a framework in which (i) mechanical stratigraphy created permeability contrasts, (ii) syn-rift normal faults established the first-order structural templates, and (iii) post-rift intraplate reactivation repeatedly modified fluid pathways and fault-seal behavior. This combination makes the Irati Formation in the studied area an exceptional natural laboratory to investigate the temporal evolution of structural traps and the role of multiepisodic brittle tectonics in controlling hydrocarbon preservation in the Paraná Basin.

MATERIALS AND METHODS

Field structural work focused on the Amaral Machado quarry exposures of the Irati Formation, emphasizing the mapping of fault zones at outcrop scale and the systematic characterization of their internal architecture. Fault traces, fault-plane kinematic indicators, and fracture corridors were mapped on high-resolution photographs and georeferenced sketch panels. Orientation measurements were collected for faults, shear fractures (R, R′, Y), joints, and veins using a Clar compass; data were subsequently processed as stereonet plots and rose diagrams to identify preferred strikes and cluster dispersion. Fault-zone architecture was described following the classical core–damage zone framework: narrow, internally brecciated fault cores versus broader, highly fractured damage zones (Caine et al., 1996; Shipton & Cowie, 2003). Systematic notes recorded the thickness and lithological makeup of fault cores (carbonate breccia, shale smear/cataclasite, calcite lenses) and the fabric, connectivity, and orientation of damage-zone fractures

(Sibson, 1990; Peacock & Sanderson, 1994).

Hydrocarbon occurrence was assessed visually and under UV light to document fluorescence and spatial restriction relative to stratigraphy and structural elements. Selected fracture fills and fault-core materials were sampled for petrography. Petrographic analysis used standard transmitted-light microscopy to identify vein textures (syntaxial/antitaxial fibrous calcite, blocky calcite, crack-seal bands), microbrecciation, dissolution seams, and stylolitic surfaces. Where appropriate, back-scattered electron (BSE) imaging and qualitative EDS checks were used to help identify compositional contrasts between calcite fills and host carbonate.

Paleostress inversion was conducted on fault-slip data and conjugate fracture sets using the WinTensor v.2.0 software to retrieve principal stress orientations and relative stress ratios based on the right-dieder method (Angelier, 1994; Michael, 1984; Delvaux & Sperner, 2003). Individual outcrop inversions were compared to evaluate internal consistency and to identify the prevailing transtensional regime.

U–Pb LA-ICP-MS geochronology targeted syntectonic calcite from vein fills and fault slickensides (Figure 3). Polished slabs were analysed following current best practice for calcite U–Pb (Roberts et al., 2017, 2020; Nuriel et al., 2017).

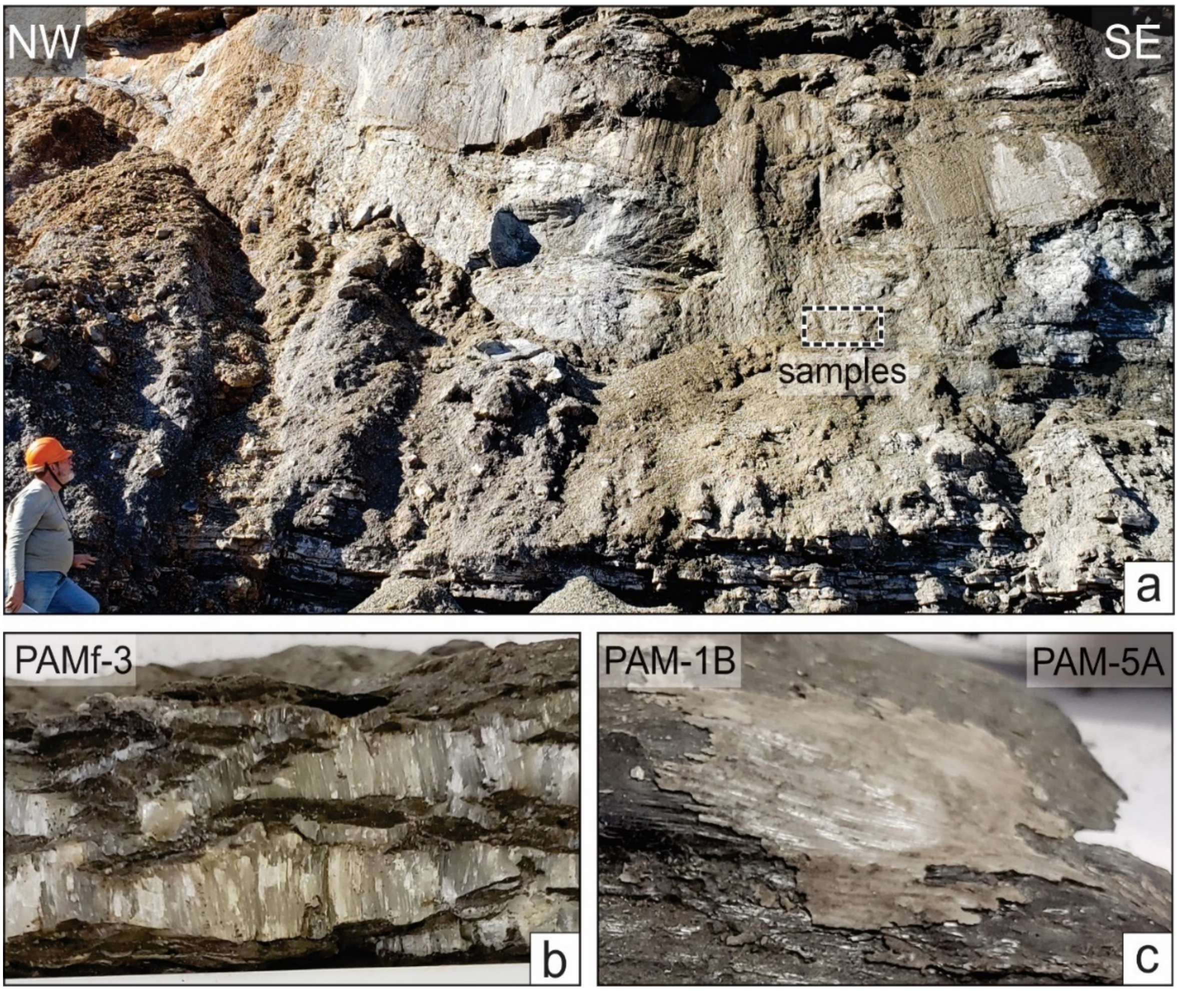

Figure 3 - Sampling location for U-Pb aging calcite; *(a)* Field view of the faulted exposure showing the sampled zone (dashed rectangle); *(b)* Sample PAMf-3, displaying banded calcite beef within the fault core; *(c)* Slickenside calcite samples PAM-1b and PAM-5a.

Spots avoided visible inclusions, solid-solution zoning, and secondary porosity. Analytical data, average element concentrations and isotopic ratios for the three analyzed samples (PAMf-3, PAM-1b and PAM-5a) are shown in table 1. Methodological details and sample datasets (including removed outliers) are provided in the Supplementary Material. Data reduction followed matrix-matched strategies using carbonate refe-rence materials (WC-1 and Duff Brown Tank limestone – Roberts et al., 2017; Hill et al., 2016) and lower-intercept ages of Tera-Wasserburg regressions were obtained with uncertainties reported at 2σ.

Ages are interpreted as vein-filling/crystallization times that bracket brittle deformation and associated fluid flow (Roberts et al., 2020).

Table 1 - U–Pb analytical data for fault-related calcite samples from the Irati Formation, including average element concentrations and isotopic ratios (see Supplementary Material for individual spot data).

Sample		U (ppm)	Pb (ppm)	Th (ppm)	$^{238}U/^{206}Pb$	$^{238}U/^{206}Pb$ (1se%)	$^{207}Pb/^{206}Pb$	$^{207}Pb/^{206}Pb$ (1se%)	n (spots)	Age (σ2se)	MSWD
PAM f-3	Calcite vein (core)	0.24	0.06	0.31	22.42	5.01	0.63	6.35	96	74.5 ± 4.2	1.4
PAM -1b	Calcite slickenside	0.63	0.04	5.61	94.64	2.33	0.41	3.59	16	37.0 ± 2.1	1.8
PAM -5a	Calcite Slickenside	1.40	0.04	5.3	155.49	1.64	0.31	3.77	5	33.0 ± 3.0	0.53

RESULTS

Fault architecture

Outcrops at the Amaral Machado quarry expose a set of NW–SE–striking normal faults dipping moderately to steeply to the southwest, with subordinate antithetic faults dipping to the northeast.

Each fault zone consists of a narrow, discontinuous core surrounded by a decameter-scale damage zone composed of densely fractured dolomitic limestone and interbedded organic-rich shale (Figure 2). Fault cores are typically decimetric in thickness and contain brecciated dolomite, shale smears and calcite (Figure 3).

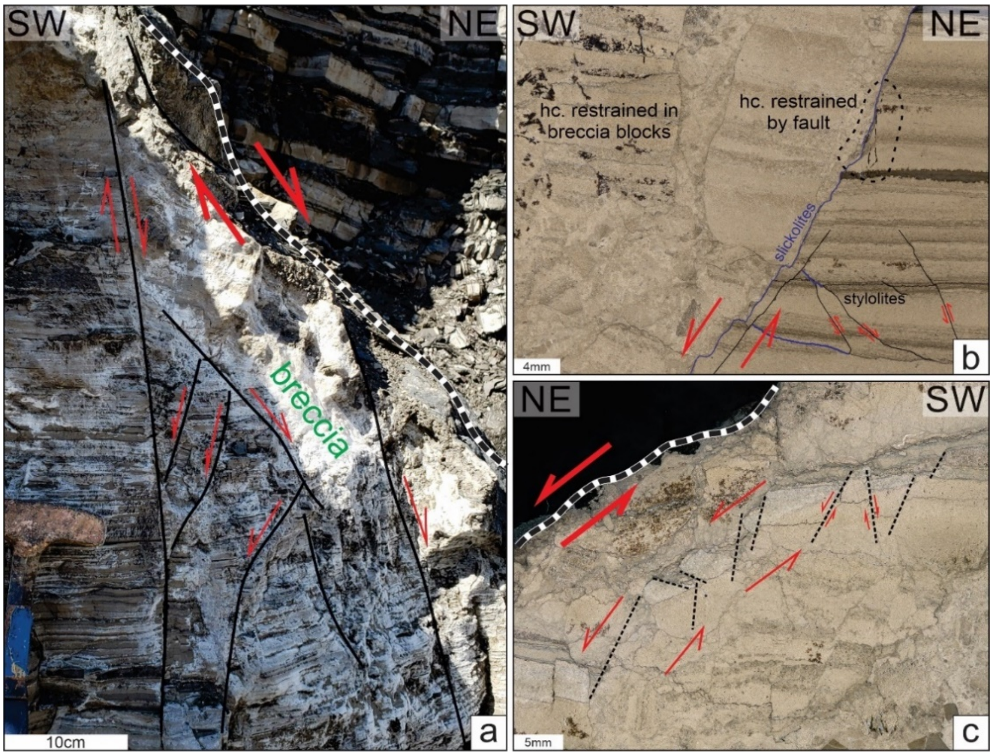

Figure 4 - Structural and microstructural characteristics of the fault-core breccia in the Irati Formation. The outcrop view *(a)* highlights intense deformation and normal-slip planes within the core zone. Photomicrographs *(b, c)* show stylolites, fracture networks and localized hydrocarbon retention, revealing the role of brecciation and stylolite formation on reducing cross-fault permeability and compartmentalizing fluid pathways.

The breccias display angular to subrounded clasts of dolomite and shale embedded in a fine matrix and have stylolites and slickolites locally, reinforcing a low permeability nature (Figure 4). Subparallel fault segments are connected by small relay ramps and stepovers, producing local dilation and fracture clustering. The structural arrangement forms an anastomosed system of Y shears and R/R′ synthetic and antithetic fractures converging toward the main planes.

Within the multilayered Irati Formation, deformation is strongly controlled by the mechanical stratigraphy: the competent dolomitic beds concentrate brittle fracturing, while the intervening shales accommodate shear and comminution, generating low-permeability seams that locally seal the system.

Damage zones display high-connectivity fracture meshes, including bedding-parallel, R/R′ shear, and T-extension fractures. Fracture density increases toward the cores, and abutting relationships indicate multiple opening episodes - early calcite-filled veins are truncated by later open fractures or those lined with thin calcite films.

Dissolution surfaces and local vuggy porosity occur along fractures within the dolomitic bank. The resulting architecture defines a laterally continuous but internally heterogeneous network that enhances both lateral and vertical fluid connectivity within the carbonate layers (Figure 5).

Figure 5 - Meso/micro scale structural control of hydrocarbon circulation in the damage zone between major faults. *(a)* shows the location of *(b)* samples at the outcrop. Hand specimens show branching fractures, dip inversion and calcite cement infill, evidencing multi-pulse brittle deformation and the progressive development of a fracture network that later evolved into a compartmentalized system.

The overall geometry delineates a NW–SE extensional fault system controlled by a NE–SW–oriented minimum principal stress (σ_3) consistent with a distributed transtensional tectonic framework compatible with the Tietê Lineament tectonic context. This structural framework provided the mechanical and hydraulic architectture that later governed hydrocarbon migration and entrapment within the Irati carbonates (Figure 6).

Hydrocarbon occurrence is restricted to fractures within the dolomitic limestone of the Irati Formation. In the fault damage zones, bitumen appears as dark impregnation films coating fracture walls and as patchy fills within open fractures. Under ultraviolet light, these fills display distinct fluorescence, confirming residual hydrocarbons confined to the carbonate layers. No impregnation is observed within the fault cores at the mesoscale, nor within shale-dominated upper intervals, even where these are in direct contact with the same fault zones. This selective distribution controls both the conduits for hydrocarbon migration (damage zone fractures) and the lateral and vertical seals of the system (shales and fault cores).

At the microscale, fibrous calcite veins occur within shale smears adjacent to fault cores. These veins show antitaxial and crack-seal fabrics with millimetric apertures, locally widening near relay zones. Bitumen occurs precisely at the calcite–shale contact and within inter-fiber spaces, locally extending toward the median line of the veins (Figure 7). This distribution suggests that hydrocarbon percolation took place during the early stages of calcite growth, implying coeval fluid flow and mineral sealing within the evolving fault zones.

Together, these features define a coupled system in which the fracture network provided transient

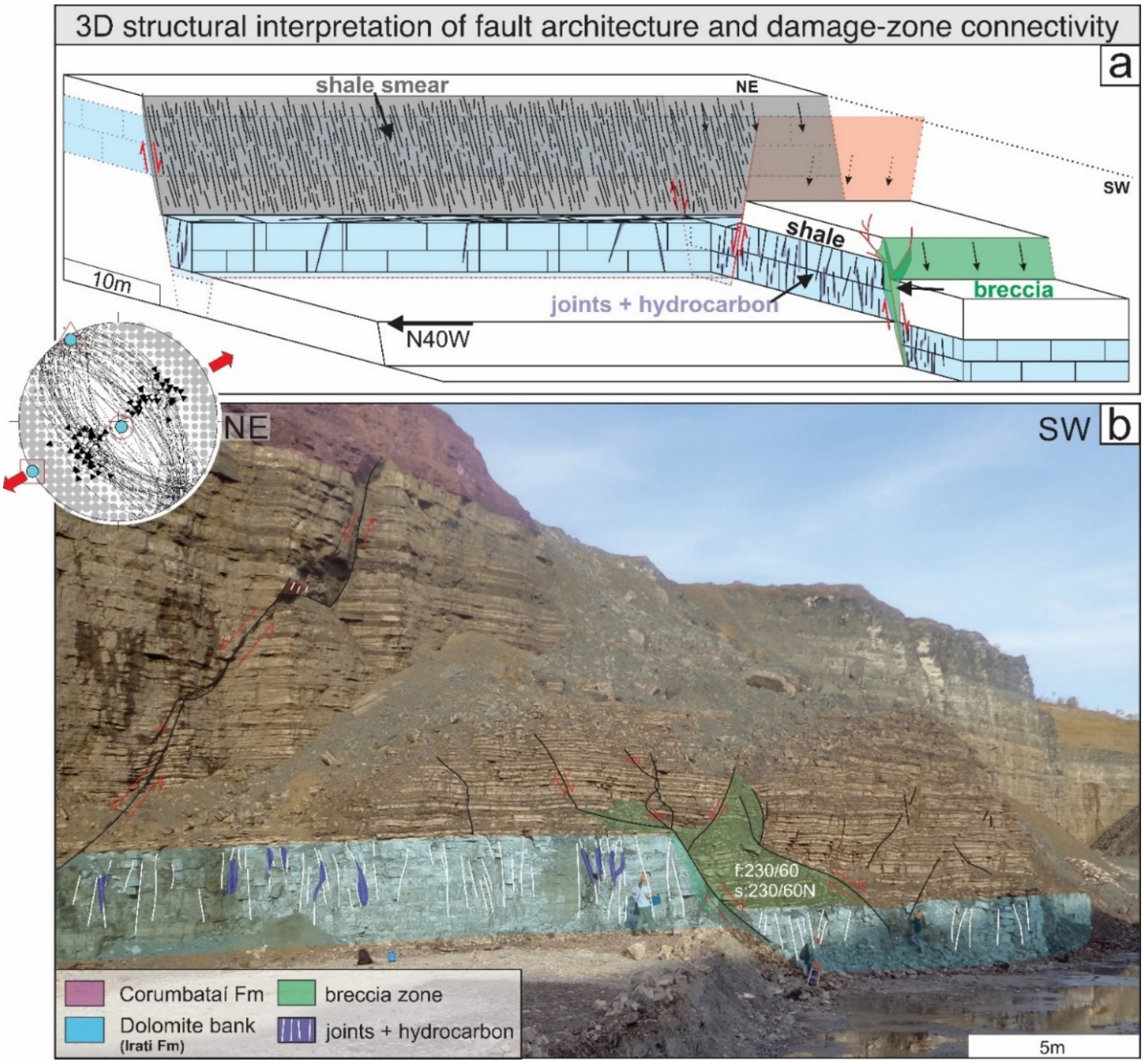

Figure 6 - 3D structural interpretation of fault architecture and damage-zone connectivity in the Irati Formation; *(a)* Conceptual block model of the outcrop showing the main structural elements of the fault zone, including shale smear, breccia core and fracture networks within the dolomitic layer; *(b)* Outcrop panorama illustrating the mapped structures corresponding to the model, highlighting hydrocarbon-bearing joints, breccia and shale-sealed segments; The stereo diagram plots fault planes, strias, and the sigma 3 position.

permeability within the dolomitic layer, while shale-rich seams and fault cores acted as effective seals. The interaction between early hydrocarbon migration and syn-tectonic calcite sealing reflects a dynamic balance between dilation, fluid influx, and progressive compartmentalization within the faulted carbonate succession.

U–Pb LA-ICP-MS data

U–Pb LA-ICP-MS analyses of syntectonic calcite from vein fills and fault slickensides yield two main age populations: the older age centers on the Late Cretaceous (~75 Ma) and was obtained from the core of the PAMf-3 antitaxial vein. The younger group clusters around ~35 Ma (Eocene), related to the samples PAM-1b and PAM-5a. Analytical uncertainties are within expected ranges for carbonate U–Pb (please refer to Supplementary Material for analytical results of each sample).

Discussion

The Saltinho region documents a structural trap whose effectiveness is fundamentally controlled by fault-zone architecture embedded in a mechanically layered carbonate–shale succession. The dolomitic bank concentrates fracture connectivity n the damage zone, whereas fault cores - enriched in shale smear/breccia and massive calcite - exhibit markedly lower permeability. This core–damage contrast is the essential ingredient that governs fluid pathways and long-term hydrocar-bon preservation. Our observations align with the classical view that damage zones act as conduits and fault cores as barriers (Sibson, 1990; Caine et al., 1996), yet the Irati case shows how that dichotomy is progressively enhanced during successsive brittle episodes within an intraplate post-rift setting (Riccomini, 1995; Zalán & Oliveira, 2005).

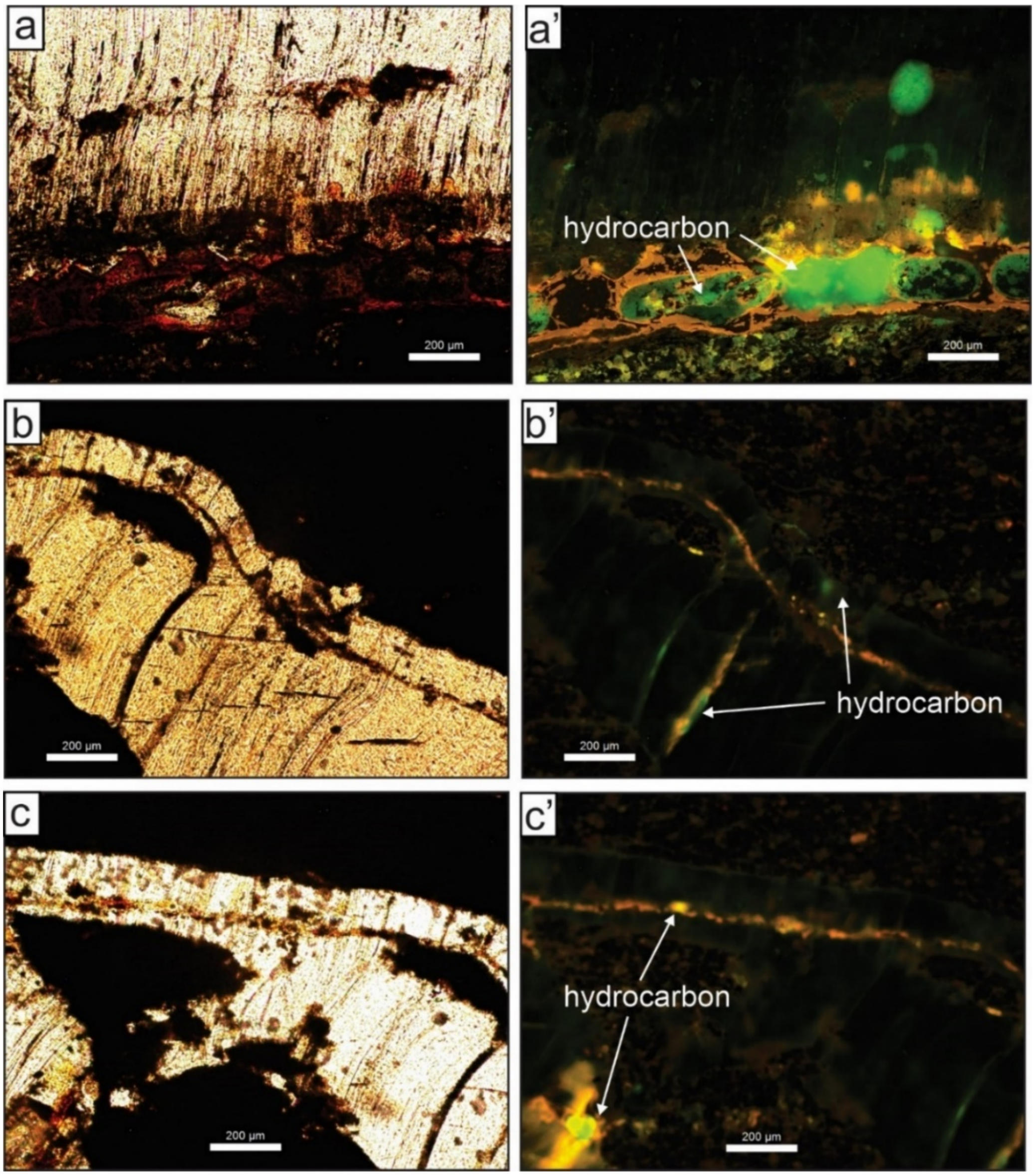

Figure 7 - Microstructural evidence of hydrocarbon retention within fracture networks of the Irati Formation. Photomicrographs under transmitted light *(a–c)* and UV fluorescence *(a'–c')* show hydrocarbons concentrated along fracture planes and micro voids in between the calcite fibres, indicating secondary porosity associated with brittle deformation.

The earliest extensional phase at ~75 Ma established a laterally continuous fracture mesh within the dolomitic bank, with linkage aided by relays, stepovers, and anastomosed R, R′ and Y shear fractures. The resulting network promoted efficient lateral flow along the carbonate layer, matching models where fracture intensity and connectivity peak near segment interactions (Peacock & Sanderson, 1994; Fossen, 2016). Crosscutting veins record repeated opening and sealing events, producing crack-seal textures typical of episodic dilation (Laubach et al., 2019). In this configuration, the damage zone provided preferential conduits that focused fluids into the dolomite horizon - precisely where hydrocarbon impregnation and UV fluorescence are found (Figure 7). The selective occurrence of hydrocarbon in the dolomitic layers, and its absence in adjacent shales and fault cores is consistent with a mechanical stratigraphy filter controlling lateral migration and local entrapment (Figure 8) (Jourde et al., 2002; Araújo et al., 2000).

The transition from conduit-dominated behavior to trap consolidation requires a permeability inversion: damage zones remain relatively open, but fault cores develop low-permeability materials - carbonate breccias, shale smears with secondary calcite - that reduce cross-fault transmissivity. In Saltinho, massive calcite lenses and shale smears within cores indicate progressive sealing.The observed fabrics are consistent with self-sealing behavior where microfracturing is limited to the core and does not reconnect to the surrouding rock, thus confining fluid-flow (Caine

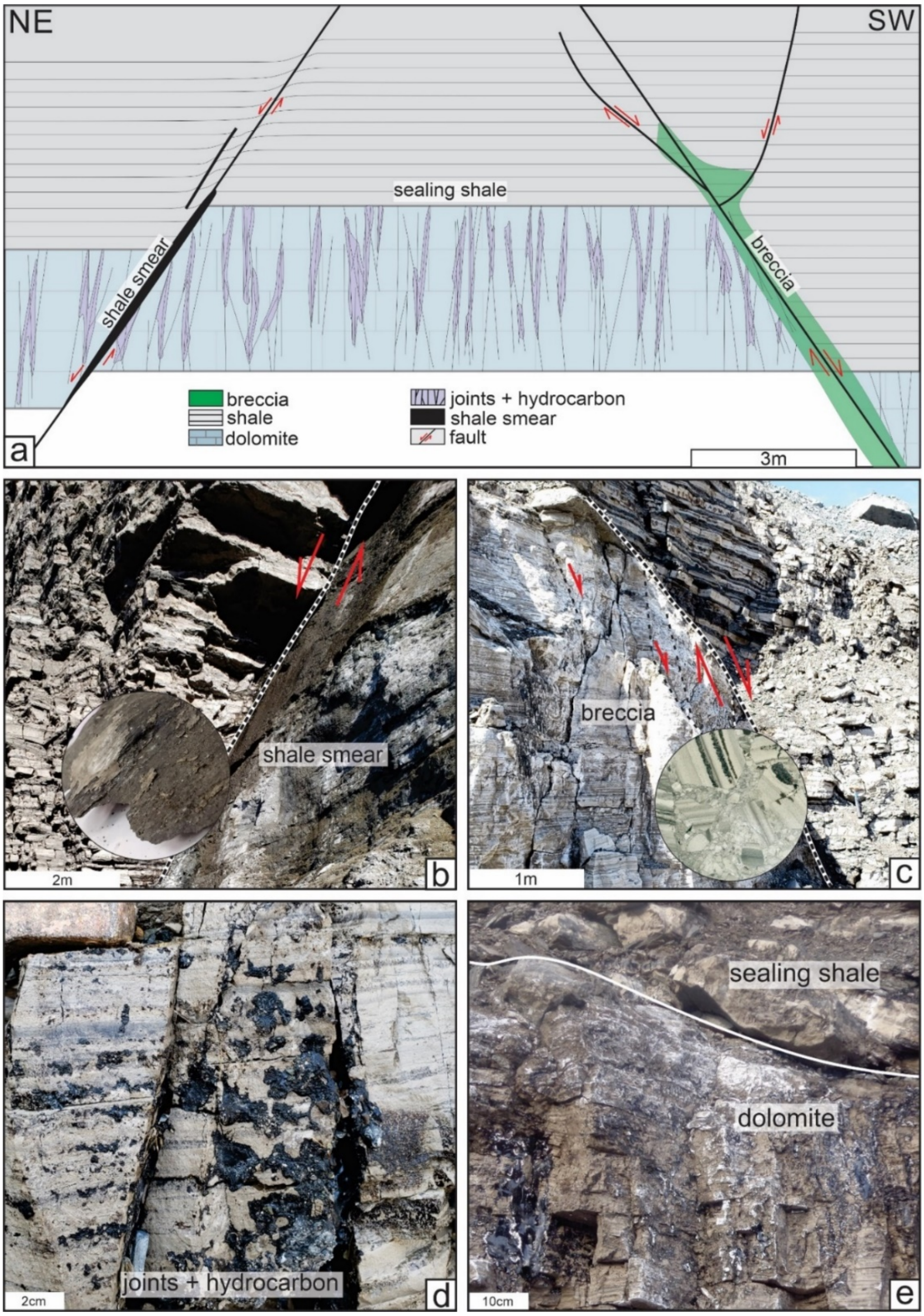

Figure 8 - Structural trap model and elements that control fault sealing and hydrocarbon trapping in the Irati Formation. *(a)* Interpretive cross-section model showing the relationship between shale smear, breccia core and joint networks within the dolomitic layer. *(b–c)* Outcrop views highlighting shale smear and breccia fault cores, reducing cross-fault permeability. *(d)* Hydrocarbon-filled joints within the damage zone, indicating early fracture-controlled migration. *(e)* Shale acting as a sealing barrier on top of the dolomite layer, completing the trapping configuration.

et al., 1996; Yielding, 2015). Stylolite formation and pressure-solution seams further contribute to permeability reduction, especially where cemented breccias border low-porosity shales (Evans, 1990; Antonellini & Aydin, 1994).

In the Irati Formation, damage zones within the dolomitic interval initially acted as laterally connected fracture corridors, focusing fluid migration along strike controlled by vertical extensional fractures while shale interbeds restricted vertical transmissivity.

This anisotropic behavior reflects the classical partitioning between conduit-dominated damage zones and low-permeability cores described in faulted carbonates elsewhere (Sibson, 1996; Caine et al., 1996; Antonellini & Aidin, 1994) and is consistent with the strong mechanical contrast between dolomite and shale.

The spatial arrangement of joints, veins, and breccias defines a permeability template that precedes trap formation, establishing the structural framework that later controlled hydrocarbon focusing and retention.

As deformation progressed, the fault core evolved into an effective barrier through brecciation, stylolitization and shale smearing, progressively reducing cross-fault transmissivity.

The textural confinement of hydrocarbons within damage-zone conduits, juxtaposed against calcite-cemented breccias and shale-rich cores, demonstrates that sealing was achieved by architectural rearrangement rather than by abrupt changes in stress or diagenetic conditions.

This pattern mirrors observations from other carbonate reservoirs in which fault-core maturation, not tectonic reactivation, dictates the transition from open to sealed systems (Caine & Minor, 2009).

Thus, by the time hydrocarbons were circulating through the fractured dolomite, the evolving core had already begun to fragment transmissivity into isolated compartments, establishing the conditions for structural trapping (Figure 8).

Petrographic observations revealed multiple cement generations whose distribution is not random: each cement pulse was confined by the evolving damage-core framework, reinforcing the fundamental role of architecture in conditioning fluid pathways through time. Paleostress analisys further shows that both the Early Createaceous syn-rift phase and the younger intraplate reactivation shared a broadly similar extensional field (σ_3 NE–SW) – possibly related to a transtensional reactivation of the Tietê Lineament in the region. Such continuity in regional stress orientation from Lower to Late Cretaceous, despite contrasting fluid behaviours, highlights that structural inheritance (weakness), rather than stress alone, is quite relevant to explain the observed selectivity of migration and trapping.

Although architecture is the primary trapping mechanism, time-dependent reactivation modulates and reinforces that control. U–Pb ages from syntectonic calcite constrain two post-rift episodes: ~75 Ma and ~35 Ma (Figure 9); we interpret the Late Cretaceous (~75 Ma) age as the stage when fault cores became effectively sealing, consolidating the trap while the damage-zone network remained the dominant lateral pathway within the dolomite.

This fits an intraplate stress field capable of reworking rift-inherited fabrics and driving fluid circulation through pre-existing conduits while cementation and cataclasis progressively reduce cross-fault flow (Riccomini, 1995; Zalán et al., 1990; Gimenez, 2024). The younger ~35 Ma event reactivated faults locally, as recorded by new microfractures and late calcite bands, but it did not reestablish connectivity across cores, implying no significant breach of the trap.

This behaviour aligns with far-field stress reorganizations recognized across the South American plate during the Paleogene, coeval with major Andean tectono-magmatic pulses (Gimenez, 2024; Gimenez et al., 2022; Santos et al., 2023; Salamuni et al., 2021; Noble et al., 1979; Sandeman et al., 1995). Intraplate responses to far-field reactivation are commonly expressed as modest brittle overprints that exploit pre-existing anisotropies (Herbozo et al., 2020) without necessarily restoring permeability. The ~35 Ma event recorded by U–Pb geochronology represents exactly this scenario: a tectonic renewal capable of reactivating fractures locally, but insufficient to overcome the mechanical and diagenetic sealing already established during the Late Cretaceous.

In this context, the three-stage evolutionary model summarized in figure 9 provides a predictive template for similar mechanically layered systems, where damage-zone connectivity governs early migration and fault-core maturation governs long-term sealing according to the following steps:

In the early syn-rift stage (~130 Ma), extensional faulting generated laterally connected fracture corridors within the dolomitic layers, establishing a conduit-dominated architecture. Fluid pathways were preferentially oriented along bedding, while intervening shale layers imposed vertical compartmentalization. Although fault cores were still immature and locally permissive, this early network defined the first-order anisotropy of fluid flow.

During the post-rift stage (~75 Ma), renewed brittle deformation and focused fluid circulation transformed the system. Calcite precipitation, breccia consolidation and shale smearing progressively reduced cross-fault permeability, allowing fault cores to evolve into low-transmissivity barriers.

From this point onward, the trap became effective: hydrocarbons were laterally supplied through damage-zone fractures but were increasingly confined within the dolomitic interval as sealing strengthened.

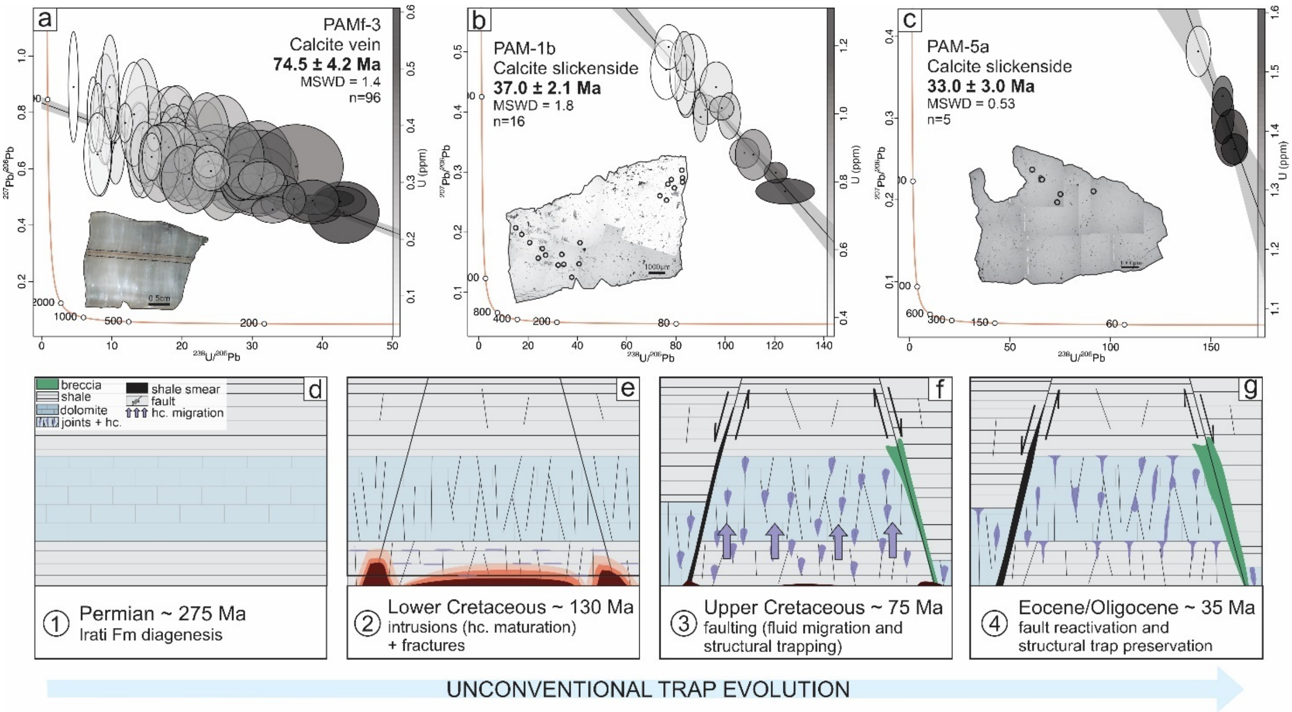

Figure 9 - U–Pb ages of syntectonic calcite and proposed evolutionary model for the unconventional structural trap in the Irati Formation. *(a–c)* Tera–Wasserburg plots showing Late Cretaceous ages associated with fault sealing and Paleogene ages linked to minor reactivation. *(d–g)* Conceptual evolution of the system: *(1)* Permian diagenesis of the Irati Formation; *(2)* Lower Cretaceous thermal influence of Serra Geral intrusions and fracture generation; *(3)* Upper Cretaceous faulting, fluid focusing and structural trap formation; *(4)* Paleogene reactivation without breaching, preserving the trap.

In the late post-rift stage (~35 Ma), a younger brittle event generated localized microfractures and minor vein growth, but this event did not reconnect previously sealed pathways. Instead of breaching the trap, this reactivation merely overprinted the existing architecture, preserving- if not reinforcing - the sealing integrity of the fault cores. As a result, permeability remained highly anisotropic, with persistent lateral continuity and long-term cross-fault isolation.

In Saltinho, architecture outweighed reactivation because the permeability structure was already "locked in" before far-field stresses were imposed, and subsequent deformation merely overprinted the pre-existing framework without dismantling it. This conclusion reinforces a broader principle for fractured carbonate reservoirs: the longevity of traps depends less on the recurrence of tectonism and more on the timing and efficiency of sealing processes relative to the establishment of conduit networks.

In unconventional systems, hydrocarbon retention and flow capacity are controlled predominantly by low-permeability architectures, capillary barriers, and mechanically guided fluid pathways, rather than by classical buoyancy-driven migration. Global syntheses emphasize that continuous or quasi-continuous accumulations near or within the source interval, characterized by ultra-low porosity and permeability, weak phase segregation, and the absence of uniform oil–water contacts - are diagnostic of unconventional behavior (Jiao, 2019; Zou et al., 2013). In Saltinho, the confinement of hydrocarbons to the dolomitic bank fit this unconventional signature: source and reservoir coincide stratigraphically (Irati Fm), transmissivity depends on secondary porosity, and long-term retention is secured by fault-core sealing rather than by a classical caprock-bounded closure.

Similar behavior has been documented in reservoir analogues where tectonic reactivation generates new fracture patterns yet sealing and fluid compartmentalization ultimately maintain – or even enhance - trap effectiveness (e.g. the western Vøring Basin, Norwegian Sea; Imber et al., 2005).

Viewed at the reservoir-to-basin scale, unified accumulation models (Pang et al., 2021) distinguish free, confined, and bound hydrocarbon dynamic fields and predict how lithological transitions govern whether accumulations behave as conventional or unconventional through time. In such classifications, Saltinho fits a hybrid structural–unconventional configuration: a self-sourced fractured carbonate in which conduit-dominated damage zones initially promoted migration, but core maturation progressively confined the system, generating a tight, structurally localized accumulation within the dolomite layer (see Figure 8).

Importantly, unconventional behavior does not preclude structural organization of the reservoir. Studies of continuous accumulations show that many conventional plays still exhibit subtle, fault-related partitioning of fluids at reservoir scale (Biddle & Wielchowsky, 1994). Thus, a reservoir can be unconventional in flow physics yet conventional in trap architecture - a duality also recognized in other fractured carbonate systems where long-term trap preservation depends on the sealing efficiency of fault cores rather than on the absence or presence of tectonic reactivation (Cant, 2011). Saltinho exemplifies this dual behavior: it is unconventional in its storage and transmissivity style and structurally organized as a compartmentalized fault-bounded trap.

This explains why the ~35 Ma reactivation event did not breach the trap: mechanical layering, fault-core sealing, and capillary barriers remained the dominant controls, while stress overprints acted only as secondary modulators.

Finally, positioning Saltinho within a global unconventional framework highlights its broader implications. Current models emphasize that continuous, self-sourced systems cluster near source rocks and within bound or confined dynamic fields, and that most yet-unrecognized petroleum volumes worldwide are expected in such configurations (Pang et al., 2021). In practice, this means that mechanical stratigraphy, core–damage evolution and sealing thresholds should guide exploration and risk assessment in fractured carbonate reservoirs.

Systems in which dolomite layers localize conduits and fault cores mature into barriers are especially prone to generating unconventional but structurally persistent traps through multi-stage tectonic histories. Future work integrating fracture modelling, reactive-transport simulations and additional carbonate geochronology could refine these controls and expand their predictive value across other intraplate settings, ultimately improving our ability to assess the stability of structural traps through geological time.

CONCLUSIONS

The integration of structural observations, microtextural evidence and U–Pb LA-ICP-MS carbonate geochronology allows us to establish a coherent evolutionary framework for the structural trap in the Irati Formation at the study area.

Our results demonstrate that trap formation and preservation were controlled by the progressive interaction between mechanical stratigraphy, damage-zone connectivity and fault-core sealing, rather than by single deformation events. Based on these observations, we summarize below the key conclusions of this study:

- The Irati Formation at Saltinho (SP) records a structural trap controlled primarily by fault-zone architecture within a mechanically layered carbonate–shale succession.
- Damage zones in the dolomitic bank formed laterally connected fracture networks that acted as conduits, while fault cores developed as low-permeability seals composed of calcite-cemented breccias and shale-rich smear/cataclasite.
- U–Pb LA-ICP-MS ages of syntectonic calcite indicate post-rift phases at ~75 Ma and ~35 Ma; the older event marks trap consolidation by core sealing, and the younger event records non-breaching reactivation.
- Architecture outweighs reactivation as the control on long-term permeability: reactivation modulates and often reinforces sealing rather than compromising it.
- The resulting three-stage model provides a predictive template for fractured carbonate systems where mechanical stratigraphy localizes conduits and seal development governs trap preservation.

ACKNOWLEDGMENTS

The authors thank M&G Mineração de Calcário Ltda staff for granting access to the Amaral Machado quarry and for sharing structural information observed during mine advancement. We also acknowledge the institutional support of UNESPetro (UNESP) and iLAMIR (UFPR) for providing full access to their staff and analytical facilities. This work was carried out with the support of the Coordination for the Improvement of Higher Education Personnel – Brazil (CAPES) – Financing Code 001 and the UNESP–Petrobras partnership (LINEAS Project), with funding provided through Fundunesp. This manuscript made limited use of artificial intelligence tools (OpenAI/ChatGPT) solely for language refinement, text organization and improvement of writing clarity. All scientific content, including data interpretation, geological discussion, and final wording choices, is the sole responsibility of the authors.

REFERENCES

ANGELIER, J. Fault slip analysis and paleostress reconstruction. **Journal of Structural Geology**, v. 16, p. 1175–1182, 1994.

ANTONELLINI, M. & AYDIN, A. Effect of faulting on fluid flow in porous sandstones: petrophysical properties. **Geology**, v. 22, n. 3, p. 925–928, 1994.

AQUAROLI, G. **Geologia e Petrografia das Impregnações Betuminosas da Região de Anhembi (SP).** Rio Claro 2013. Dissertação (Mestrado), Instituto de Geociências e Ciências Exatas, Universidade Estadual Paulista, Rio Claro,

ARAÚJO, L.M.; TRIGUIS, J.A.; CERQUEIRA, J.R.; SANTOS NETO, E.V. Hydrocarbon accumulation and dolomitization in the Irati Formation. **AAPG Bulletin**, v. 84, p. 1–20, 2000.

BARBOSA, O. & ALMEIDA, F. F. M. – A série Tubarão na bacia do rio Tietê, Estado de São Paulo. Rio de Janeiro. Bol. **Div. Geol. Min. – D.N.P.M**., **Notas preliminares,** 1949.

BASTOS, L.P.H.; RODRIGUES, R.; PEREIRA, E.; BERGAMASCHI, S.; ALFERES, C.L.F.; AUGLAND, L.E.; SVENSEN, H.H. The birth and demise of the vast epicontinental Permian Irati-Whitehill sea: evidence from organic geochemistry, geochronology, and paleogeography. **Palaeogeography, Palaeoclimatology, Palaeoecology**, v. 562, p. 110103, 2021.

BIDDLE, K.T. & WIELCHOWSKY, C.C. Hydrocarbon traps. In: MAGOON, L. B.; DOW, W. G. (Eds.). The Petroleum System — From Source to Trap. **AAPG Memoir,** v. 60. Tulsa: American Association of Petroleum Geologists, 1994. p. 219-235.

CAINE, J.S. & MINOR, S.A. Structural and geochemical characteristics of faulted sediments and inferences on the role of water in deformation, Rio Grande Rift, New Mexico. **Geological Society of America Bulletin,** v. 121, n. 9–10, p. 1325–1340, 2009.

CAINE, J.S.; EVANS, J.P.; FORSTER, C.B. Fault zone architecture and permeability structure. **Geology,** v. 24, n. 11, p. 025–1028, 1996.

CANT, D. "**Unconventional" hydrocarbon accumulations occur in conventional traps.** CSPG CSEG CWLS Convention, p. 1–2, 2011.

CERRI, R.I.; LUVIZOTTO, G.L.; TOGNOLI, F.M.W.; WARREN, L.V.; OKUBO, J.; MORALES, N. Mechanical stratigraphy and structural control of oil accumulations in fractured carbonates of the Irati Formation, Paraná Basin, Brazil. **Brazilian Journal of Geology**, v. 50, n. 2, p. 1–18, 2020.

CPRM – Serviço Geológico do Brasil. **Mapa Geológico do Estado de São Paulo. Escala 1:750.000**. Brasília: CPRM, 2019.

DAEMON R.F. & QUADROS, L.P. Bioestratigrafia e Palinologia do Paleozoico Superior da Bacia do Paraná. Ponta Grossa. PETROBRÁS/DESUL. 1 v.; **Relatório Interno nº 384**, 1969.

DELVAUX, D. & SPERNER, B. Stress tensor inversion from fault kinematic indicators and focal mechanism data: the TENSOR program. In: NIEUWLAND, D. (Ed.) **New Insights into Structural Interpretation and Modelling**. Geological Society, London, Special Publications, v. 212, p. 75-100, 2003.

EVANS, J.P. Textures of fault rocks and implications for permeability. **Geological Society of America Bulletin**, v. 102, n. 5, p. 124–135, 1990.

FOSSEN, H. **Structural Geology.** 2nd Ed. Cambridge University Press, 2016. 528 pp.

GIMENEZ, V.B. **Geomorfologia tectônica e datação de falhas por geocronologia U-Pb (LA-ICP-MS) em carbonatos: reativações pós-rifte na região do Lineamento Rio Piquiri, sul do Brasil.** Rio Claro, 2024. Tese (Doutorado em Geociências) – Instituto de Geociências e Ciências Exatas, Universidade Estadual Paulista.

GIMENEZ, V.B.; SALAMUNI, E.; DOS SANTOS, J.M.; PEYERL, W.R.L.; FARIAS, T.F.S.; SANCHES, E. The role of fault reactivation in the geomorphological evolution of coastal landforms on passive continental margins: evidence from a tectonic estuary in southern Brazil. **Geomorphology,** v. 402, p. 108132, 2022.

HACKSPACHER, P.C.; HADLER NETO, J.C.; TASSINARI, C.C.G.; ALMEIDA, M.E.; FUKUMURA, F.T.; RODRIGUES, S.W.O. Intraplate reactivation in SE Brazil. **Journal of South American Earth Sciences**, v. 16, p. 725–739, 2004.

HERBOZO, G.; KUKOWSKI, N.; CLIFT, P. D.; PECHER, I.; BOLAÑOS, R. Cenozoic increase in subduction erosion during plate convergence variability along the convergent margin off Trujillo, Peru. **Tectonophysics**, v. 790, p. 228557, 2020.

HILL, C.A.; POLYAK, V.J.; ASMEROM, Y.; PROVENCIO, P. Constraints on a Late Cretaceous uplift, denudation, and incision of the Grand Canyon region, southwestern Colorado Plateau, USA, from U–Pb dating of lacustrine limestone. **Tectonics**, v. 35, n. 4, p. 896–906, 2016.

IMBER, J.; HOLDSWORTH, R.E.; MCCAFFREY, K.J.W.; WILSON, R.W.; JONES, R.R.; ENGLAND, R.W.; GJELDVIK, G. Early Tertiary sinistral transpression and fault reactivation in the western Vøring Basin, Norwegian Sea: implications for hydrocarbon exploration and pre-breakup deformation in ocean margin basins. **AAPG Bulletin**, v. 89, n. 8, p. 1043–1069, 2005.

JIAO, F. Re-recognition of "unconventional" in unconventional oil and gas. **Petroleum Exploration and Development**, v. 46, n. 5, p. 847–855, 2019.

JOURDE, H.; MANGOLD, N.; ANDRÉ, G.; CROIZE, D.; HAMEUR, H.; ZWILLER, N.; HIRSCH, F. Fracture flow in layered carbonates. **Water Resources Research**, v. 38, p. 1287, 2002.

LAUBACH, S.E.; HILDREBRANDT, P.; WILKINSON, M.; FALL, A. Fracture networks in carbonates: attributes and diagenesis. **AAPG Bulletin**, v. 103, p. 1–36, 2019.

LISBOA, V.A. **Geoquímica Orgânica e Potencial Gerador da Formação Irati na Borda Leste da Bacia do Paraná, São Paulo.** São Paulo. 2006.Tese (Doutorado), Instituto de Geociências, Universidade de São Paulo, São Paulo.

MATEUS, A.M.; RICCOMINI, C.; FERREIRA, E.; TASSINARI, C.G. Permian-Triassic maturation and multistage migration of hydrocarbons in the Assistência Formation (Irati Subgroup), Paraná Basin, Brazil: implications for the exploration model. **Brazilian Journal of Geology**, v. 44, n. 3, p. 355–360, 2014.

MICHAEL, A.J. Determination of stress from slip data. **Journal of Geophysical Research**, v. 89, n. B13, p. 11517–11526, 1984.

MILANI, E.J. **Evolução tectono-estratigráfica da Bacia do Paraná e seu relacionamento com a geodinâmica fanerozoica do Gondwana Sul – ocidental.** 255 p. 1997. Tese (Doutorado em Geociências). Instituto de Geociências, Universidade Federal do Rio Grande do Sul. Porto Alegre.

MILANI, É.J.; FRANÇA, A.B.; SCHNEIDER, R.L. Bacia do Paraná. **Boletim de Geociências da Petrobrás**, v. 8, n. 1, p. 69–82, 1994.

MILANI, E.J.; MELO, J.H.G.; SOUSA, P.A.; FERNANDES, L.A.; FRANÇA, A.B. Bacia do Paraná. **Boletim de Geociências da Petrobrás**, v. 15, n. 2, p. 265–287, 2007.

MORAES REGO, L.F.A Geologia do Petróleo no Estado de São Paulo. **Boletim do Serviço Geológico e Mineralógico do Brasil,** v. 46, p. 1–80, 1930.

NOBLE, D.C.; MCKEE, E.H.; MÉGARD, F. Early Tertiary "Incaic" tectonism, uplift, and volcanic activity, Andes of central Peru. **Geological Society of America Bulletin**, v. 90, n. 10, p. 903–907, 1979.

NURIEL, P.; ROBERTS, N.M.W.; BLAIR, P.; RHODES, F.C.; DRURY, M.R. U–Pb dating of calcite: constraints on brittle deformation. **Geology**, v. 45, n. 2, p. 531–534, 2017.

PANG, X.; JIA, C.; CHEN, J.; LI, M.; WANG, W.; HU, Q.; GUO, Y.; CHEN, Z.; PENG, J.; LIU, K.; WU, K. A unified model for the formation and distribution of both conventional and unconventional hydrocarbon reservoirs. **Geoscience Frontiers,** v. 12, n. 2, p. 695–711, 2021.

PEACOCK, D.C.P. & SANDERSON, D.J. Geometry of relay ramps. **Journal of Structural Geology**, v. 16, n. 2, p. 57–72, 1994.

PERINOTTO, J.A.J. & ZAINE, M.F. **Patrimônios Naturais e História Geológica da Região de Rio Claro-SP.** Rio Claro: Arquivo Público e Histórico do Município de Rio Claro, v.1. 2008.

RICCOMINI, C. Tectonic reactivation in SE Brazil. R**evista Brasileira de Geociências**, v. 25, n. 14, p. 271–276, 1995.

ROBERTS, N.M.W.; WALKER, R.J.; DARRAH, R.; HODSON, K.; WILKINSON, J.J. U–Pb geochronology of calcite using LA-ICP-MS: method refinement and applications. **Chemical Geology**, v. 467, n. 6, p. 76–89, 2017.

ROBERTS, N.M.W.; DARRAH, R.; WALKER, R.J.; HODSON, K.; MAAS, R.; WILKINSON, J.J. Calcite U–Pb geochronology. **Chemical Geology**, v. 532, n. 7, p. 119340, 2020.

SALAMUNI, E.; SILVA, C.L; NASCIMENTO, E.R.; SANTOS, J.M.; PEYERL, W.R.L.; GIMENEZ, V.B. Morphometric and structural diagnosis of fault reactivation in the Cenozoic: a case study of the Blumenau–Soledade Lineament in southern Brazil. **Brazilian Journal of Geology**, v. 51, n. 3, p. e20200080, 2021.

SANDEMAN, H.A.; CLARK, A.H.; FARRAR, E. An integrated tectono-magmatic model for the evolution of the southern Peruvian Andes (13–20°S) since 55 Ma. **International Geology Review**, v. 37, n. 12, p. 1039–1073, 1995.

SANTOS, R.V.; SOUZA, P.A.; DE ALVARENGA, C.J.S.; DANTAS, E.L.; PIMENTEL, M.M.; DE OLIVEIRA, C.G.; DE ARAÚJO, L.M. SHRIMP U–Pb zircon dating and palynology of bentonitic layers from the Permian Irati Formation, Paraná Basin, Brazil. **Gondwana Research,** v. 9, n. 4, p. 456–463, 2006.

SANTOS, J.M.; SALAMUNI, E.; MORALES, N.; CASTRO, L.G.; SILVA, C.L.; SOUZA, I.A.; OLIVEIRA, S.P. Aeromagnetic and structural characterization of dyke swarms in southeast Brazil: evidence for Cenozoic reactivation of the Guapiara lineament, Ponta Grossa Arch. **Journal of South American Earth Sciences**, v. 129, p. 104523, 2023.

SCHNEIDER, R.L.; MULMANN, H.; TOMMASI, E.; MEDEIROS, R.A.; DAEMON, R.F.; NOGUEIRA, A.A. Revisão Estratigráfica da Bacia do Paraná. In: CONGRESSO BRASILEIRO DE GEOLOGIA, Porto Alegre. 1974. **Anais.**.. Porto Alegre: Sociedade Brasileira de Geologia, 1974.

SHIPTON, Z.K. & COWIE, P.A. Damage and core structure: implications for seals. **Journal of Structural Geology**, v. 25, n. 1, p. 1515–1534, 2003.

SIBSON, R.H. Conditions for fault-valve behaviour. Geological Society, London, **Special Publications**, v. 54, n. 1, p. 15–28, 1990.

SIBSON, R.H. Crustal stress, faulting and fluid flow. Geological Society, London, **Special Publications,** v. 78, n. 1, p. 69–84, 1994.

SIBSON, R.H. Structural permeability of fluid-driven fault–fracture meshes. **Journal of Structural Geology**, v. 18, n. 8, p. 1031–1042, 1996.

SIMÕES, M. G. & FITTIPALDI, F. C. **Fósseis da região de Rio Claro.** Arquivo do Município de Rio Claro, 77 p, 1992.

SOARES, P.C. Irati stratigraphy and depositional setting. **Revista Brasileira de Geociências**, v. 18, p. 242–252, 1988.

SOARES, P.C. Elementos estruturais da parte nordeste da Bacia do Paraná: classificação de gênese. In: CONGRESSO BRASILEIRO DE GEOLOGIA, 28. Porto Alegre. **Anais.**...Porto Alegre: Sociedade Brasileira de Geologia, v. 1, p. 107-121, 1974.

THOMAZ FILHO, A.; MILANI, E.J.; RANGEL, H.D. Magmatismo nas bacias sedimentares brasileiras e sua influência nos sistemas petrolíferos. **Revista Brasileira de Geociências**, v. 38, n. 2, p. 200–219, 2008.

YIELDING, G. Fault seal analysis in siliciclastic and carbonate reservoirs. Geological Society of London, **Special Publications**, v. 421, p. 1–20, 2015.

ZALÁN, P.V. & OLIVEIRA, J.A.B. Tectonics of Brazil's southeast margin. **Boletim de Geociências da Petrobras,** v. 13, p. 149–196, 2005.

ZALÁN, P.V.; CONCEIÇÃO, J.C.J.; WOLFF, S.; ASTOLFI, M.A.M.; VIEIRA, I.S.; APPI, C.J. The Paraná Basin and South Atlantic rifting. **Tectonophysics**, v. 198, p. 191–221, 1990.

ZOU, C.N.; YANG, Z.; TAO, S. Z.; YUAN, X.J.; ZHU, R.K.; HOU, L.H.; PANG, Z.L. Continuous hydrocarbon accumulation over a large area as a distinguishing characteristic of unconventional petroleum: the Ordos Basin, North-Central China. **Earth-Science Reviews,** v. 126, p. 358–369, 2013.

Submetido em 29 de outubro de 2025
Aceito para publicação em 28 de maio de 2026

SUPPLEMENTARY MATERIAL 1

U-PB LA-ICP-MS METHOD

In situ U-Pb geochronology via Laser Ablation Inductively Coupled Mass Spectrometry (LA-ICP-MS) was conducted at the iLAMIR Institute (Curitiba, PR, Brazil), we used a **Teledyne/Photon Machines Analyte Excite 193nm excimer** laser ablation system coupled to an **Thermo iCap-RQ quadrupole ICP-MS** (Table 1).

The U-Pb LA-ICP-MS method for carbonates (Li et al., 2014; Coogan et al., 2016) is adapted from that used for zircons (Spencer et al., 2014), with a few modifications. Standard sample bracketing used the NIST612 glass for normalisation of $^{207}Pb/^{206}Pb$ ratios (Woodhead & Hergt, 2007). After correction of $^{207}Pb/^{206}Pb$ ratios, an in-house carbonate reference material (WC-1) of known age (254 ± 7 Ma; isotope dilution U-Pb data from Roberts et al., 2017) is used for normalisation of U^{238}/Pb^{206} ratios. The Duff Brown Tank limestone (Hill et al., 2016) was used as a secondary reference material during each analytical session. No downhole correction was made, instead the mean of each 30s ablation (excluding the first 2s of data) was used.

Normalisation is based on the measured/accepted ratio derived from the session-based drift-corrected mean of the primary WC-1 reference material. Each session refers to a morning or afternoon, i.e. 2-3 hours of analyses. Data are not corrected for common lead. Obtained ages are deemed robust (based on low MSWD, < 2) and were determined from lower intercepts on Tera-Wasserburg (i.e. total Pb/U isochron) plots. While adjusting the Roberts et al. (2017) method to ensure age reproducibility at the LAMIR Institute (UFPR), we have made several changes in the analytical setup – mainly on pre ablation settings (2 s) and several combinations of detectors configurations until optimum sensibility was reached.

Table 1: Analytical conditions at the iLAMIR Institute (UFPR).

Laboratory & Sample Preparation	
Laboratory name	iLAMIR Institute
Sample type/mineral	Calcite
Sample preparation	Chips mounted in 2.5cm epoxy mounts
Imaging	Scanning Electron Microscopy (SEM-BSE)
Laser ablation system	
Make, Model & type	Teledyne/PhotonMachines Analyte Excite, 193nm, Excimer
Ablation cell & volume	Dual-mode discrete dynode electron multiplier
Laser wavelength (nm)	193nm
Pulse width (ns)	4ns
Fluence (J.cm^{-2})	~7 J/cm^{-2}
Repetition rate (Hz)	10 Hz
Spot size (□m)	100 µm
Sampling mode / pattern	Static spot
Carrier gas	100% He, Ar make-up gas
Ablation duration (secs)	15secs
Cell carrier gas flow (l/min)	0.6l/min
ICP-MS Instrument	
Make, Model & type	Thermo iCap-RQ quadrupole ICP-MS
Sample introduction	Ablation aerosol
RF power (W)	1300W
Make-up gas flow	0.7l/min Ar
Detection system	Single Mascom SEM
Masses measured	202, 204, 206, 207, 208, 232, 238
Integration time per peak (ms)	Dwell times of 200 µs to 1000 µs per peak
Total integration time per reading (secs)	0.35 sec (should represent the time resolution of the data)
Sensitvity / Efficiency (%, element)	~0.2% U
IC Dead time (ns)	15 ns
Data Processing	
Gas blank	30 second on-peak zero subtracted
Calibration strategy	See text.
Reference Material info	See text.

Data processing package used / Correction for LIEF	In-house spreadsheet data processing after initial signal integration using Iolite v.4. No LIEF correction (mean of uncorrected ratios used). Tera-Wasserburg plots were made using IsoplotR (Ludwig, 2003; Vermeesch, 2018).
Mass discrimination	Standard sample bracketing
Common-Pb correction, composition and uncertainty	None applied. Ages calculated from regressions used in Tera Wasserburg plots.
Uncertainty level & propagation	Ages are quoted at 2sigma absolute, propagation is by quadratic addition. Excess variance of reference material propagated into sample data. Systematic uncertainties include age uncertainty of reference material.

REFERENCES

COOGAN, L.A., PARRISH, R.R., ROBERTS, N.M.W. Early hydrothermal carbonates from the upper oceanic crust: implications for the global carbon cycle and ocean chemistry. Earth and Planetary Science Letters, 449, 337–347. 2016;

HILL, C.A., POLYAK, V.J., ASMEROM, Y., PACES, J.B., DUCHENE, H.R., MCINTOSH, W.C. Dating late Quaternary speleothems and cave carbonates from the Guadalupe Mountains, New Mexico, USA. Geosphere, 12(6), 1839–1862. 2016;

LI, Q., PARRISH, R.R., HORSTWOOD, M.S.A., MCARTHUR, J.M. U–Pb dating of cements in Mesozoic sandstones: constraints on the timing of diagenetic cementation and fluid flow. Chemical Geology, 385, 134–149. 2014;

LUDWIG, K.R. User's Manual for Isoplot 3.00: A Geochronological Toolkit for Microsoft Excel. Berkeley Geochronology Center Special Publication 4, 70 pp. 2003;

ROBERTS, N.M.W., RASBURY, E.T., PARRISH, R.R., SMITH, C.J., HORSTWOOD, M.S.A., CONDON, D.J. A calcite reference material for LA–ICP–MS U–Pb geochronology. Geochemistry, Geophysics, Geosystems, 18(7), 2807–2814. 2017;

SPENCER, C.J., KIRKLAND, C.L., TAYLOR, R.J.M. Strategies towards statistically robust interpretations of in situ U–Pb carbonate data. Geoscience Frontiers, 5(4), 473–486. 2014;

VERMEESCH, P. IsoplotR: a free and open-source toolbox for geochronology. Geoscience Frontiers, 9(5), 1479–1493. 2018;

WOODHEAD, J.D., HERGT, J.M. Application of the NIST SRM 610 glass as a calibration standard in laser ablation ICP–MS analysis. Geostandards and Geoanalytical Research, 31(4), 331–343. 2007.

Suplementary Material 2

^{238}U/^{206}Pb	^{238}U/^{206}Pb (1se%)	^{207}Pb/^{206}Pb	^{207}Pb/^{206}Pb (1se%)	Outliers *	Spots	^{204}Pb	^{206}Pb	^{207}Pb	^{208}Pb	^{232}Th	^{238}U	Th/U	Uppm	Pbppm	Thppm
6,30106483	19,9414609	0,692512349	10,71615222	X	PAMf_3-1	639	725	510	1505	2083	4872	0,42746	0,131322	0,10558	0,141914919
4,52697862	6,339138519	0,89037302	8,891138604		PAMf_3-2	613	379	335	871	1163	1871	0,621223	0,05044	0,068666	0,079217154
13,8980268	5,324524866	0,702405382	7,749060261		PAMf_3-3	586	456	319	713	3428	6853	0,500204	0,184715	0,064799	0,233584814
10,537374	5,288384392	0,692512349	8,573761587		PAMf_3-4	589	434	299	731	2724	4932	0,552296	0,13294	0,064135	0,185619102
14,1082843	4,35319621	0,672726281	8,090707644		PAMf_3-5	582	598	400	1032	3741	9053	0,413171	0,244017	0,081619	0,254884965
9,05395723	7,306231579	0,811228751	9,758147346		PAMf_3-6	579	420	333	736	2125	4092	0,51936	0,110291	0,064604	0,144811587
18,5768445	5,807967472	0,643047181	9,232935643		PAMf_3-7	611	484	306	801	1971	9621	0,204903	0,259324	0,068822	0,134333567
9,07157194	3,985115705	0,741977516	6,669665992		PAMf_3-8	575	435	323	810	1329	4246	0,312979	0,114437	0,066947	0,090546934
9,61399582	7,755203821	0,752859853	3,487998852		PAMf_3-9	669	438	331	788	1823	4572	0,398644	0,123234	0,069525	0,124196252
9,14272152	7,866053776	0,781549651	11,39416048	X	PAMf_3-10	609	411	306	780	1530	4017	0,380913	0,108269	0,065815	0,104261644
9,97387802	4,372908912	0,814196661	5,896466957		PAMf_3-11	533	370	305	816	1593	3969	0,401221	0,106988	0,063237	0,108521129
8,18032978	10,10554702	0,771656617	10,25836007	X	PAMf_3-12	591	399	300	714	1916	3552	0,539563	0,095732	0,062612	0,130585139
16,8028395	7,770945577	0,702405382	7,749060261		PAMf_3-13	541	405	283	766	2534	7331	0,345661	0,197593	0,062338	0,172669614
8,40141977	7,681127574	0,662833248	9,703553857		PAMf_3-14	586	458	301	810	2455	4168	0,589041	0,112347	0,067338	0,167302158
6,80698974	6,596686162	0,850800885	16,28029829	X	PAMf_3-15	599	410	328	803	2233	2989	0,746945	0,080567	0,06683	0,152138092
9,71414161	5,242779426	0,89037302	8,335732988		PAMf_3-16	561	370	328	850	3208	3891	0,824526	0,104865	0,065893	0,218589737
5,48563291	32,35850433	0,810239448	6,108281227	X	PAMf_3-17	650	810	721	1760	3969	4871	0,814907	0,131289	0,12316	0,270476956
14,8025015	9,542690807	0,771656617	6,413375651		PAMf_3-18	607	433	333	757	5324	7037	0,75664	0,189671	0,066557	0,36281395
13,8773452	3,988836507	0,682619315	10,14689877	X	PAMf_3-19	623	423	290	779	6091	6336	0,961422	0,170775	0,066066	0,415079351
7,34297319	4,762357047	0,791442684	6,877908476		PAMf_3-20	590	399	315	731	3518	3165	1,111388	0,085319	0,063588	0,239719536
15,7793163	5,363614349	0,679651405	7,208015398		PAMf_3-21	544	474	320	881	5974	8059	0,741287	0,217214	0,06933	0,407068711
13,960443	5,348134428	0,672726281	9,560915608		PAMf_3-22	540	405	269	741	4363	6054	0,720727	0,163175	0,061089	0,297316277
7,97057774	5,163185822	0,781549651	6,332273136		PAMf_3-23	550	418	327	742	3179	3586	0,886549	0,096642	0,06364	0,216602069
8,18032978	16,23915828	178,0746039	100,0002	X	PAMf_3-24	645	460	78053	873	4152	4108	1,010652	0,110729	2,500685	0,282916751
11,8045265	12,04027557	0,603475047	10,65761446	X	PAMf_3-25	614	466	276	816	4201	5985	0,701821	0,161328	0,067869	0,286239981
16,8031688	5,730976665	0,730292812	10,13710828	X	PAMf_3-26	664	343	243	607	2770	5940	0,46633	0,147753	0,051645	0,18254432
22,9458366	5,106129003	0,720423991	6,852234446		PAMf_3-27	636	356	258	606	2940	8420	0,349169	0,209442	0,0517	0,193747401
18,5314947	7,168012846	0,7697681	6,413375651		PAMf_3-28	653	319	244	551	1970	6110	0,322422	0,151982	0,049143	0,129823939
19,2654153	9,128650372	0,641473416	15,38591533	X	PAMf_3-29	693	346	208	569	2140	6850	0,312409	0,170389	0,050588	0,14102702
27,2521981	3,967203108	0,562522842	4,390522544		PAMf_3-30	673	409	234	548	3800	11450	0,331878	0,284811	0,051784	0,250421811

15,2016168	9,394180379	0,690817525	12,14450409	X	PAMf_3-31	654	339	220	551	3280	5360	0,61194	0,133326	0,049032	0,216153564
25,7381871	6,377493337	0,700686347	9,157113932		PAMf_3-32	643	380	264	591	3800	10030	0,378863	0,249489	0,052256	0,250421811
13,7028658	3,780313175	0,618775126	7,81755079		PAMf_3-33	597	353	222	519	1960	4970	0,394366	0,123625	0,047003	0,129164934
17,5297923	7,052595894	0,759899278	11,04077266	X	PAMf_3-34	628	320	231	597	2640	5760	0,458333	0,143276	0,049365	0,173977258
11,4729183	5,868019493	0,878325139	10,67603082	X	PAMf_3-35	697	297	257	597	1860	3520	0,528409	0,087558	0,051422	0,122574887
17,5931912	3,755294636	0,643447181	7,517998177		PAMf_3-36	638	358	232	562	2800	6510	0,430108	0,161932	0,049755	0,184521335
19,2273414	5,959136418	0,759899278	7,145656594		PAMf_3-37	681	324	245	509	2453	6410	0,382683	0,159444	0,048921	0,161653869
28,2820777	4,978150747	0,523047555	14,15235666	X	PAMf_3-38	664	418	216	508	3120	12130	0,257214	0,301725	0,050171	0,205609487
7,84599575	31,45733546	0,848718674	9,304475333	X	PAMf_3-39	627	390	410	564	2160	3080	0,701299	0,076613	0,055314	0,14234503
11,4459232	11,19256426	0,784571332	6,166766057	X	PAMf_3-40	701	470	352	830	2720	5370	0,506518	0,133575	0,06532	0,179249297
7,97461863	9,854348582	0,651342238	9,093108825		PAMf_3-41	610	298	187	534	2310	2460	0,939024	0,061191	0,045307	0,152230101
24,6304677	4,847403195	0,61581448	7,935213119		PAMf_3-42	657	342	210	534	6380	8720	0,731651	0,216904	0,048448	0,420445041
12,9720463	34,00529371	0,580286721	6,550672881	X	PAMf_3-43	650	540	320	930	6280	7360	0,853261	0,183075	0,06671	0,413854994
19,5362143	6,353694621	0,700686347	7,045092949		PAMf_3-44	631	334	231	581	7200	6790	1,060383	0,168897	0,049477	0,474483432
20,7000739	4,613649126	0,690817525	10,0019998	X	PAMf_3-45	653	302	211	541	5550	6430	0,863142	0,159942	0,047475	0,365747646
28,1185975	6,818358137	0,601998129	9,838098697		PAMf_3-46	580	391	234	551	7440	11430	0,650919	0,284313	0,048837	0,490299547
23,729353	8,557645103	0,582260486	6,61319444		PAMf_3-47	589	425	245	634	7100	10420	0,681382	0,25919	0,052534	0,467893384
19,8957765	10,14046561	0,690817525	10,0019998	X	PAMf_3-48	563	333	218	625	6090	6800	0,895588	0,169145	0,048365	0,401333903
18,39137	6,266973375	0,680948703	11,59592777	X	PAMf_3-49	598	276	182	564	3720	5250	0,708571	0,13059	0,045029	0,245149773
6,35884623	6,563429934	0,759899278	13,63783022	X	PAMf_3-50	613	294	211	521	2150	1920	1,119792	0,047759	0,045585	0,141686025
19,9066664	4,397966711	0,686022913	6,722628864		PAMf_3-51	720	417	281	688	4080	8690	0,469505	0,208984	0,055016	0,241738689
20,6789078	3,07632013	0,723694691	7,536900653		PAMf_3-52	700	404	293	628	3100	8720	0,355505	0,209706	0,052926	0,183674004
21,1810446	3,582608878	0,591843467	6,535724138		PAMf_3-53	674	431	254	646	2290	9610	0,238293	0,231109	0,052377	0,135681764
15,1819829	3,610332572	0,612662081	4,939325878		PAMf_3-54	706	431	264	641	3620	6840	0,52924	0,164494	0,053344	0,214483837
25,0522538	7,465403548	0,643394321	7,167659884		PAMf_3-55	708	471	295	645	4140	12360	0,334951	0,297243	0,054598	0,245293669
15,7812717	4,074029771	0,70386744	4,159740352		PAMf_3-56	659	414	291	672	4480	6840	0,654971	0,164494	0,052821	0,26543856
30,9516555	5,997828258	0,634472058	8,596076958		PAMf_3-57	662	437	271	636	4160	14180	0,293371	0,341012	0,05243	0,246478663
17,3822703	3,940870527	0,687014275	6,712936693		PAMf_3-58	634	371	249	638	2300	6720	0,342262	0,161608	0,049399	0,136274261
20,502165	4,527116052	0,664212936	8,211391226		PAMf_3-59	669	398	261	639	4170	8510	0,490012	0,204655	0,051358	0,24707116
18,7769339	4,540793677	0,693953814	7,8596879		PAMf_3-60	659	373	255	623	4010	7320	0,547814	0,176037	0,049896	0,237591211
14,4069268	7,232139084	0,743521943	13,33483325		PAMf_3-61	724	371	261	670	3180	5550	0,572973	0,133471	0,05303	0,188413978
27,4928745	5,05009621	0,509560372	5,15951981		PAMf_3-62	708	441	226	595	3090	12660	0,244076	0,304458	0,051437	0,183081507
20,7235707	3,827024187	0,68503155	5,285984656		PAMf_3-63	660	350	238	651	3180	7600	0,418421	0,182771	0,049608	0,188413978

21,1343903	7,293444063	0,60473118	9,018611352		PAMf_3-64	689	498	291	672	4380	10890	0,402204	0,261892	0,056165	0,259513592
20,0732494	3,709927811	0,657273398	6,71489465		PAMf_3-65	658	378	245	635	4170	7940	0,525189	0,190948	0,050157	0,24707116
19,1135721	4,226076458	0,689988363	5,463432045		PAMf_3-66	662	393	269	652	5000	7840	0,637755	0,188543	0,051594	0,296248393
43,0269651	4,746594809	0,445121803	9,912930912		PAMf_3-67	640	490	214	633	9470	22090	0,428701	0,531238	0,051646	0,561094456
25,5186522	5,485042937	0,565076677	10,52821562		PAMf_3-68	648	425	238	675	7840	11390	0,688323	0,273916	0,051985	0,46451748
21,2279053	5,233621809	0,643394321	6,782610375		PAMf_3-69	637	369	232	624	9020	8200	1,1	0,1972	0,048642	0,534432101
21,3697399	4,825863003	0,576973028	5,931208005		PAMf_3-70	623	354	204	563	6450	7930	0,813367	0,190707	0,045559	0,382160427
28,9006422	3,367142041	0,628523883	7,258276503		PAMf_3-71	646	371	230	591	9640	11180	0,862254	0,268866	0,048015	0,571166902
22,5765017	4,510671698	0,567059402	7,957059343		PAMf_3-72	655	396	219	567	6800	9360	0,726496	0,225097	0,048067	0,402897815
30,7532475	6,917097251	0,555163051	8,930811148		PAMf_3-73	646	380	201	525	8580	12300	0,697561	0,295801	0,045768	0,508362242
13,1438537	6,466253173	0,793090073	9,377133091		PAMf_3-74	645	272	209	519	3010	3610	0,833795	0,086816	0,043104	0,178341533
18,7037295	3,944535282	0,62356707	5,806307238		PAMf_3-75	676	323	202	547	5931	6330	0,936967	0,152229	0,045664	0,351409844
31,1396428	2,654894746	0,546518203	4,384126332		PAMf_3-76	540	349	192	464	3120	12090	0,258065	0,420864	0,061178	0,253559774
35,0019241	5,652091884	0,638269434	10,93932842	X	PAMf_3-77	519	320	196	434	2600	12410	0,209508	0,432004	0,058318	0,211299812
30,3036793	5,235834368	0,571450602	3,32190743		PAMf_3-78	577	309	176	441	4130	10430	0,395973	0,363078	0,059589	0,335641624
25,2955082	3,00175266	0,566464122	3,438919298		PAMf_3-79	614	325	183,8	484	3420	9100	0,375824	0,31678	0,0638	0,277940522
23,2146438	5,687265209	0,648242394	5,234591364		PAMf_3-80	571	292	187	430	3170	7520	0,421543	0,261778	0,058795	0,257623232
22,3527139	4,373040026	0,656220762	2,894456023		PAMf_3-81	620	314	206	506	3750	7790	0,481386	0,271177	0,065548	0,304759344
24,7410861	3,072845495	0,603364074	3,0643848		PAMf_3-82	558	323	195	493	2890	8860	0,326185	0,308425	0,06229	0,234867868
32,4838001	4,358047264	0,531558763	3,008531295		PAMf_3-83	531	330	175	408	4510	12000	0,375833	0,417731	0,057364	0,366523904
17,5690592	6,254526608	0,642258618	7,145656594		PAMf_3-84	547	272	173	510	2880	5300	0,543396	0,184498	0,059589	0,234055176
17,6033069	5,00684105	0,695115305	4,09384096		PAMf_3-85	543	242	168	470	4290	4780	0,89749	0,166396	0,05649	0,348644689
30,8208069	7,532467003	0,588404634	10,171458	X	PAMf_3-86	548	307	175	460	3830	10600	0,361321	0,368996	0,059192	0,311260877
29,4152978	4,761084855	0,567461418	3,871601609		PAMf_3-87	549	304	172	450	4870	10010	0,486513	0,348458	0,058596	0,395780801
33,822084	7,327975494	0,638269434	15,62627995	X	PAMf_3-88	579	299	179	482	3220	11310	0,284704	0,393712	0,061138	0,26168669
19,2547898	5,046456526	0,571450602	6,111475852		PAMf_3-89	554	313	176	420	3090	6680	0,462575	0,232537	0,058119	0,251121699
28,3977875	3,976345946	0,56945601	5,782794071		PAMf_3-90	568	294	167	418	3960	9260	0,427646	0,322349	0,057484	0,321825867
41,8078538	2,616032268	0,493661515	2,331825128		PAMf_3-91	544	364	179,8	434	8080	16830	0,480095	0,585868	0,060423	0,6566548
36,2670539	7,453906531	0,608350554	9,838098697		PAMf_3-92	563	283	164,6	433	5842	11410	0,512007	0,397193	0,057325	0,474774423
23,5783196	5,515759599	0,708080153	9,157113932		PAMf_3-93	579	255	174	422	4510	6690	0,674141	0,232885	0,056808	0,366523904
18,0971872	8,93799715	0,676166681	5,313499845		PAMf_3-94	576	267	181	426	3810	5450	0,699083	0,18972	0,057603	0,309635493
14,683734	5,560918794	0,657218058	6,679777787		PAMf_3-95	574	258	166,3	410	5090	4210	1,209026	0,146554	0,055934	0,413660016
16,69223	6,957527672	0,618323514	8,873222001		PAMf_3-96	553	385	231	620	5640	7120	0,792135	0,247854	0,07111	0,458358053

20,0677698	17,7878999	0,747971993	18,00111108	X	PAMf_3-97	620	360	239	590	8200	8220	0,997567	0,286146	0,071904	0,666407099
21,501182	25,00719896	0,485683147	7,702802234	X	PAMf_3-98	624	460	198	488	7070	10270	0,688413	0,357508	0,070315	0,57457295
11,8822321	3,602942011	0,762931432	3,665590932		PAMf_3-99	551	218	167	435	3460	2890	1,197232	0,100604	0,054464	0,281191288
21,2983406	10,39468947	0,688134233	9,422412693	X	PAMf_3-100	532	250	168	374	4950	5960	0,830537	0,207473	0,052438	0,402282334
16,0293949	2,597058941	0,708361115	2,609644224		PAMf_3-101	1422	538	382	971	3760	8270	0,454655	0,146164	0,060388	0,168838204
36,0937754	3,330356181	0,476225897	2,935690923		PAMf_3-102	1491	681	325	794	6770	23570	0,28723	0,416577	0,060059	0,303998574
20,4038886	2,984901875	0,630650613	3,165881334		PAMf_3-103	1505	544	343	849	4600	10630	0,432738	0,187875	0,059111	0,206557377
38,7673884	3,934902386	0,442352089	3,384293201		PAMf_3-104	1449	690	306	792	6800	25700	0,264591	0,454223	0,059056	0,305345688
28,1376206	3,810969313	0,5798399	3,184979835		PAMf_3-105	1495	546	317	761	6200	14790	0,419202	0,261399	0,056885	0,278403421
29,7363491	3,741602857	0,536999495	3,438104093		PAMf_3-106	1459	617	332	824	7290	17630	0,4135	0,311593	0,058928	0,327348539
23,7890793	15,92040117	0,515081148	6,869449776	X	PAMf_3-107	1430	680	327	797	5470	15400	0,355195	0,27218	0,058928	0,245623664
31,2453578	14,93742827	0,476225897	3,875457009	X	PAMf_3-108	1361	740	346	777	9750	22300	0,43722	0,394131	0,058746	0,437811832
34,2065192	2,841839085	0,531021764	3,476676712		PAMf_3-109	1459	591	314	784	7710	19370	0,398038	0,342346	0,057451	0,346208125
24,285835	3,075339262	0,575854746	2,947968628		PAMf_3-110	1367	493	284	741	7260	11520	0,630208	0,203605	0,052725	0,326001426
20,9763424	7,538944011	0,563899284	8,747869609		PAMf_3-111	1389	735	410	1020	4810	15000	0,320667	0,265111	0,064766	0,21598717
29,1565317	10,60194984	0,62566917	4,6221634	X	PAMf_3-112	1520	680	427	880	6100	19100	0,319372	0,337574	0,064037	0,273913043
42,5495727	3,506991779	0,484196205	4,428386935		PAMf_3-113	1378	637	306	788	10480	25900	0,404633	0,457758	0,056721	0,470591589
33,1240344	2,295008971	0,550947534	2,629678007		PAMf_3-114	1376	542	299	753	6540	17140	0,381564	0,302933	0,054167	0,293670706
31,0599255	3,172972543	0,575854746	4,329881047		PAMf_3-115	1382	547	317	779	7650	16300	0,469325	0,288087	0,055279	0,343513899
34,5451976	3,842512959	0,48120734	5,076405094		PAMf_3-116	1293	608	291	751	12500	20140	0,620655	0,355955	0,053638	0,56129722
38,9115051	3,033899031	0,473237032	2,954146342		PAMf_3-117	1300	574	272	750	9960	21430	0,464769	0,378755	0,052908	0,447241625
38,6243353	3,920720659	0,486188782	6,150793457		PAMf_3-118	1262	635	308	760	13640	23580	0,578456	0,416754	0,054002	0,612487527
32,9157072	3,665788216	0,455303839	4,162356981		PAMf_3-119	1263	614	278	741	13290	19300	0,688601	0,341109	0,052835	0,596771205
23,7351358	3,45387515	0,626665459	3,741438392		PAMf_3-120	1240	403	252	682	10230	9180	1,114379	0,162248	0,04707	0,459365645
28,8352476	4,039301081	0,627661747	8,732449339		PAMf_3-121	1237	635	399	970	14490	17510	0,827527	0,309473	0,059111	0,650655738
15,6929458	3,50008663	0,642606075	5,275110583		PAMf_3-122	1220	440	280	732	6260	6640	0,942771	0,117356	0,048712	0,281097648
31,3389068	4,234341875	0,564895573	4,325613749		PAMf_3-123	1333	501	282	684	9880	15200	0,65	0,268645	0,051083	0,443649323
24,1179605	4,532972071	0,591795362	4,718045663		PAMf_3-124	1191	439	260	668	9540	10230	0,932551	0,180805	0,046668	0,428382038
35,9944803	1,821076161	0,492166513	4,559044867		PAMf_3-125	1196	580	285	738	12850	20000	0,6425	0,353481	0,051083	0,577013542

*Outliers with uncertainties (1se) > 10% were removed. Spot PAMf-3-24 was also disconsidered on the calculations of average values shown in Table 1 (main article) due to its extremely high uncertainties.

Spots were concentrated in the median zone of the vein.